An evaluation of the regional distribution and wet deposition of secondary inorganic aerosols and their gaseous precursors in IFS-COMPO Cycle 49R1.

Jason E. Williams [1], Swen Metzger [2], Samuel Rémy [3], Vincent Huijnen [1] and Johannes Flemming [4]

1 R&D Weather and Climate Modeling, Royal Netherlands Meteorological Institute, De Bilt, the Netherlands

2 ResearchConcepts Io, Freiburg, Germany

3 HYGEOS, Lille, France

4 European Centre for Medium-Range Weather Forecasts, Bonn, Germany

Abstract

Secondary Inorganic Aerosol (SIA) makes up a considerable fraction of the total particulate matter exposure and, thus, is an important product from any forecasting system of atmospheric composition and air quality. The subsequent loss to the surface of SIA via dry and wet deposition determines the duration of the exposure time for humans and the extent of acidification imposed on sensitive ecosystems. Here we provide a description and evaluation of the most recent updates made towards aerosol production, aerosol scavenging and wet deposition components of the global IFS-COMPO chemical forecasting system, which is used as part of the Copernicus Atmosphere Monitoring Service. The application of the EQSAM4Clim simplified thermodynamic module in IFS-COMPO cycle 49R1 changes the efficacy of phase transfer of SIA precursor gases (Sulphur dioxide, Nitric Acid and Ammonia) which significantly impacts the concentrations of the respective SIA particulate concentrations by changing the fraction converted into SIA. Comparisons made against observational composites at the surface for Europe, the U. S. and South-East Asia during 2018 show reductions in the global annual mean bias statistics for both sulphates and nitrates. Updating the IFS-COMPO model towards cycle 49r1 increases both the burden and lifetime of sulphate and ammonium particles by one third. Coupling EQSAM4Clim into IFS-COMPO provides a better description of the partitioning between state phases involving ammonia and ammonium across regions, whereas changes for sulphate are minimal. For nitric acid and nitrates, the partitioning changes significantly, leading to lower particulate concentrations and a corresponding increase in gas-phase nitric acid with an associated improvement in surface nitrate. There is also a shift in the size of particles towards the fine mode nitrate away from the coarse mode. The impact on the total regional wet deposition values is generally positive, except for sulphates in the U.S. and ammonium particles in South-East Asia which are strongly influenced by the precursor emission estimates. This provides confidence that cycle 49r1 IFS-COMPO has the ability to provide accurate deposition fluxes of S and N at global scale.

1 Introduction

The SIA occurs throughout the troposphere, where resident concentrations are dependant on Temperature (T), Relative Humidity (RH) and the concentrations of inorganic precursor gases, namely water vapour (H_2O), Sulphur Dioxide (SO_2) Ammonia (NH_3) and Nitric Acid (HNO_3). High concentrations of SIA contribute to total Particulate Matter concentrations that accumulate in various size bins of 1.0μm (PM1.0), 2.5μm (PM2.5) and 10μm (PM10) (Liu et al, 2022), and have detrimental effects on both human health and visibility (Sharma et al, 2020; Ting et al., 2021). The main types of SIA are ammonium sulphate ($(NH_4)_2SO_4$), ammonium bisulphate (NH_4HSO_4) and ammonium nitrate (NH_4NO_3). Once formed, the sulphates are very stable and deposit to the surface, whereas NH_4NO_3 is more unstable and can decompose back to the precursor gases (Feick and Hainer, 1954) depending on T and RH. These particles can be transported out of source regions subsequently influencing air quality in neighboring countries (e.g., Vieno et al., 2014; Chang et al., 2022). Anthropogenic activity makes a significant contribution to SIA formation via the emission of NO_x (oxidised nitrogen in the form NO and NO_2), NH_x (reduced nitrogen) and SO_2, where there has been a general trend of decreasing Sulphur (S) and Nitrogen (N) emissions in the EU, US and China (Tørseth et al., 2012; Aas et al., 2019; Benish et al., 2022; Jiang et al., 2022) resulting in an increasing fraction of SIA being from NH_4NO_3. This results in a decrease in the lifetime of SIA, due to the increased meteorological instability of NH_4NO_3 (e.g. Williams et al., 2015; Metzger et al., 2002; 2006), reducing the potential for reduced long-range transport out of the source regions (He et al., 2018).

At RH values above 50%, most SIA take up water and exist in a deliquescent state. At high RH values SIA formation is enhanced (Gao et al., 2020) therefore, under constant or changing emissions, SIA is likely to become more ubiquitous in a warming atmosphere. The hygroscopic growth of SIA alters both the optical properties (in terms of scattering and absorption) and interactions with gas-phase trace species via changes in pH (e.g. Jayne et al., 1990; Shi et al, 2018). The concentrated salt solution produced typically has higher ionic strength with cloud droplets with pH values ranging between -1 to 6 (Ault, 2020). The high solubility of SIA results in the scavenging into aquated aerosols and clouds being a dominant loss term. This has impacts in terms of the acidification of sensitive ecosystems and an increase in eutrophication due to high nitrogen loading in inland water bodies, which can result in the exceedance of critical loads for vegetation (e.g. Sun et al., 2020). The uptake of carbon to land is also enhanced with an increase in N loading (Holland et al., 1997; Reary et al., 2008). Once dissolved in solution, SIA dissociates efficiently into the respective ionic constituents (e.g. nitrate (NO_3^-), ammonium (NH_4^+) and sulphate ($SO_4^=$)) whereas these anions/cations are deposited on land during precipitation events.

A distinct difference exists with respect to the main source terms for the various SIA species. For NO_x and NH_x species, particle formation is sensitive to the resident gas-phase precursor species, temperature and RH, in the absence of aqueous phase droplets. For SO_4^{2-}, production occurs almost exclusively in the aqueous phase after SO_2 is scavenged into cloud and fog, whose cumulative oxidation rate is dependent on the prescribed pH in solution. Recent studies have shown that the correct prescription of cloud pH is necessary to account for changes in SO_4^{2-} efficacy over long time scales for the determination of trends (Thurock et al., 2019; Myriokefalitakis et al., 2022). The representation of acidity in tropospheric aerosols and clouds ranges significantly across large-scale atmospheric models. The most simplistic representation is to use a fixed cloud water pH of between 5.0-5.6, thus effectively representing the impact of dissolved carbon dioxide (CO_2). A more accurate representation includes the influence of other dissolved species which either acidify (e.g. HNO_3, H_2SO_4) or buffer (e.g NH_3) solution pH once scavenged via irreversible uptake. This is the approach adopted in the Integrated Forecasting System with atmospheric composition extension (IFS-COMPO) for both cloud and precipitation. Other SO_4^{2-} production terms involving e.g. methyl-hydroperoxide (CH_3OOH) have been shown to be of secondary importance towards the total SO_4^{2-} production (Myriokefalitakis et al., 2022). The more buffering of solution by NH_3, the faster the conversion rate as dictated by the reaction of HSO_3^- being less than that for $SO_3^=$ (Warneck, 1991).

One dominant loss term for SIA is wet deposition in precipitation to the surface. Previous global tropospheric modelling studies have been performed focusing on the temporal accuracy and annual deposition totals at continental scale for NH_x and SO_x (Zhang et al., 2012; Kanikadou et al., 2016; Ge et al., 2021), as well as multi-model intercomparison studies to examine the variability across different models and the main assumptions causing such differences (Dentener et al., 2006; Bain et al., 2017; Tan et al., 2018). The accuracy of any model towards capturing the correct wet deposition terms is a balance between the accuracy of the precursor emission inventory, the distribution of the cloud liquid water content (defining the cloud Surface Area Density, SAD), the representation of the formation and distribution of aerosol particles, the extent of phase-transfer and the parametrizations adopted for describing dry/wet deposition to the surface.

The IFS-COMPO model is a large-scale global model used for operational analyses and air quality forecasts (Peuch et al, 2022; Williams et al., 2022; Rémy et al., 2024) used in the Copernicus Atmosphere Monitoring Service (CAMS). This service provides forecasts and reanalysis of trace gases and aerosols for the purpose of informing

108 national service providers and policy makers. It currently provides chemical/aerosol forecast products, among
109 them Ozone (O_3), Nitrogen Dioxide (NO_2), SO_2, PM2.5, PM10 and also Aerosol Optical Depth. One main focus
110 of the recent updates made to IFS-COMPO is the reduction of biases and increase in correlation for aerosol
111 products (Rémy et al., 2024). In that, acidic deposition and N-loading can also be output from the model means
112 such that improving the deposition term via an improved distribution in PM will foster the development of this
113 IFS-COMPO future product.

114 In this paper we present an analysis of the regional performance of IFS-COMPO Cy48r1 and Cy49r1 towards the
115 surface distributions N and S gaseous precursors for SIA and the associated particle concentrations and
116 distributions as evaluated against ground based observation networks, with special focus on the application of
117 latest update of EQSAM4Clim (Metzger et al., 2024) in the global chemical forecasting model IFS-COMPO
118 Cy49r1. This work is complementary to the recent evaluation of the performance of IFS-COMPO Cy48r1 and
119 Cy49r1 and of the impact of using EQSAM4Clim with respect to regional PM2.5 distributions and Aerosol Optical
120 Depth presented in Rémy et al (2024). The influence on regional wet and dry deposition terms are subsequently
121 evaluated to assess upgrades to both EQSAM4Clim and the deposition schemes. In Sect. 2 we provide details of
122 the IFS-COMPO simulations used, a brief description of the latest model updates and emissions used. In Sect 3
123 we describe the observational networks against which the surface evaluations are performed for the precursor gases
124 and resulting SIA particulates. In Sect. 4 we provide details of the changes in regional surface concentrations of
125 precursor gases and associated particulates and regional annual mean statistics and in Sect 5., we present the
126 associated comparisons of the annual mean wet deposition fluxes for Europe, the U. S. and South-East Asia and
127 discuss improvements. Finally, in Sect. 6 we present some further discussion and conclusions from our study.
128 Additional information in support of the main findings are also given in the supplementary material.

129 **2 Model description of IFS-COMPO versions**

130

131 The IFS-COMPO global composition model (previously known as C-IFS) is used for operational air quality
132 analyses and forecasts as part of CAMS. The modelling and data assimilation framework is regularly updated.
133 During 2023 IFS-COMPO was based on the Cy48r1 version of IFS, and uses recently updated chemical and
134 aerosol components for the near-real time simulations of atmospheric composition (
135 https://www.ecmwf.int/en/elibrary/81374-ifs-documentation-cy48r1-part-viii-atmospheric-composition ; last
136 access 20 February 2024; Rémy et al., 2022; Williams et al., 2022), but since end of 2024 has moved to the Cy49r1
137 version. IFS-COMPO Cy49r1 has been shown to improve on the evaluated biases simulated in previous cycles for
138 key products such as O_3 and NO_2 (Huijnen et al., 2016; Huijnen et al., 2019; Williams et al. 2022;
139 https://atmosphere.copernicus.eu/eqa-reports-global-services ,last access 17 February 2025). For this study we
140 perform simulations with both Cy48r1 and a version of IFS-COMPO pertaining to Cy49r1, which is now
141 operational. These updates were included to improve the aerosol component, the wet deposition scheme and the
142 description of pH in clouds and aerosols by applying the EQSAM4Clim approach and other updates related to
143 cloud scavenging (Metzger et al, 2016; Metzger et al., 2024; Remy et al., 2024). For brevity we only provide a
144 brief description of the updates made to the IFS-COMPO aerosol/chemistry component, wet deposition
145 parameterization and the implementation of EQSAM4Clim into IFS-COMPO which determines surface deposition
146 fluxes here. A more comprehensive description of Cy49r1 updates is provided in Rémy et al. (2024) and of the
147 EQSAM4Clim thermodynamic module in Metzger et al. (2024), along with a schematic showing the interaction
148 of these different models towards providing accurate air quality forecasts.

149

150 **2.1 Updates in IFS-COMPO Cy49r1**

151 IFS-COMPO Cy49r1 is built on the previous operational cycle (Cy48r1) and contains 8 distinct aerosol types with
152 multiple bins for size segregation, namely sea salt, desert dust, organic carbon, black carbon, $SO_4^=$, fine and coarse
153 NO_3^-, NH_4^+ and Secondary Organic Aerosol. For Cy49r1 updates have been made to the aerosol component of the
154 model in the form of modifying both the description and properties of Desert Dust and Sea-Salt. This impacts the
155 resident lifetimes and long-range transport component for each aerosol species. Modifications to the description
156 of the aerosol optics has also been implemented, which improves the simulation with respect to the Aerosol Optical
157 Depth (AOD) and Ångström exponent when compared against regional observations (Rémy et al., 2024). The gas-
158 phase chemistry, photolysis and dry deposition are identical to that described in Williams et al. (2022).

159 For Cy49r1 there has been an integration of the aerosol and chemistry components in the code to make them more
160 consistent, where both the sulfur and nitrogen cycles are now represented through the aerosol module (for
161 particulate species) and the chemistry module (for gaseous species and aqueous $SO_4^=$ production). The aerosol
162 module also provides additional input to the chemistry module to better represent heterogeneous reactions (via

195 Surface Area Density (SAD)) and the effects of aerosols on photolysis rates. The extent of gas–particle partitioning
196 and conversion via heterogeneous reactions on dust and sea-salt particles, are outlined in Rémy et al. (2019), as
197 based on the work of Hauglustaine et al. (2014). In Cy48r1, the first version of the EQuilibrium Simplified Aerosol
198 Model (EQSAM; Metzger et al., 2002) was implemented for the calculation of e.g. NH_4NO_3 concentrations. These
199 parameterizations rely on meteorological data provided by IFS, as well as gaseous precursors such as nitric HNO_3
200 and NH_3 from the chemistry module. The gas–particle partitioning scheme estimates compound production
201 through the neutralization of HNO_3 by NH_3 left over after sulfuric acid neutralization. It also accounts for the
202 formation of specific compounds from heterogeneous reactions of HNO_3 with calcite (found in dust aerosol) and
203 sea-salt particles.

204 In IFS-COMPO Cy49r1, EQSAM4Clim is used to estimate the gas/particle partitioning of the HNO_3-NO_3^- and
205 NH_3-NH_4^+ couples and to provide an estimate of the aerosol pH. The pH of aqueous solutions, aquated aerosols
206 and precipitation is now updated each time-step using the EQSAM4Clim approach accounting for additional
207 cations (Ca^{2+}, Mg^{2+}, Na^+, K^+), anions ($SO_4^=$, HSO_4^-, NO_3^-, Cl^-) and their solute interactions, whose methodology
208 is comprehensively described in Metzger et al. (2012, 2016, 2024). This replaces the original estimate of solution
209 pH determined by summing the contributions from dissolved CO_2 and strong acids (HNO_3, HSO_3^-, H_2SO_4, NO_3^-
210 and Methane Sulfonic Acid) which is buffered by dissolved NH_3. The contribution towards solution pH of
211 dissolved Formic and Acetic acid (HCOOH and CH_3COOH, respectively) are also now accounted for in Cy49r1,
212 which has been shown to contribute to the pH in cloud droplets (Shah et al., 2020). This impacts the phase-transfer,
213 speciation and subsequent aqueous-phase oxidation of SO_2 in cloud droplets (thus impacting $SO_4^=$). Also the loss
214 of gas-phase species such as e.g. H_2O_2 and the corresponding formation of SIA particles is affected. Note that both
215 the original (Cy48r1) and updated (Cy49r1) approaches account for the most dominant gaseous contributions
216 towards solution pH, namely SO_2, HNO_3 and NH_3. This means that differences imposed in cloud pH are naturally
217 less than the associated changes in aerosol pH.

218 Below cloud scavenging of gaseous precursors is also affected by the pH of solution (e.g. Seinfeld and Pandis,
219 2006). In Cy48r1 fixed values for cloud pH are used over land (pH=5.0) and ocean (pH=5.6), thus only providing
220 limited variability with respect to regions affected by both high and low emissions. In Cy49r1 this has been updated
221 such that the calculator of the pH is coupled to resident trace gas and aerosol concentrations to improve consistency
222 within IFS-COMPO and to provide variable scavenging rates dependent on tropospheric composition.

223 In Cy48r1, the wet deposition routines for aerosols and chemistry in IFS-COMPO are distinct, though both utilise
224 a scheme adapted from Luo et al. (2019), which is used operationally. To ensure a consistent approach between
225 aerosol and trace gases wet deposition, and to simplify code maintenance, these separate implementations have
226 been merged into a unified routine. This new routine now represents the wet deposition processes for both aerosols
227 and chemical species and is called with either chemical or aerosol tracers as input. Similar to Cy48r1 and previous
228 versions, the routine in Cy49r1 is executed twice: once for large-scale precipitation and once for convective
229 precipitation. In the case of convective precipitation, the assumed precipitation fraction has been standardised to
230 0.05 (whereas in Cy48r1 a value of 0.1 was used for chemistry scavenging and 0.05 for aerosol scavenging).

231 Additional upgrades have been made for aerosol wet deposition as follows: (i) The aerosol activation
232 parameterization of Verheggen et al. (2007) has been implemented. This parameterization estimates the fraction
233 of aerosols that can be scavenged through in-cloud processes as a function of temperature. It is applied to mixed
234 clouds, specifically for temperatures between the freezing point and 233K. For temperatures above 0°C, the
235 consistency of the parameters determining the fraction of aerosols subject to in-cloud wet deposition with the
236 results of the Verheggen parameterization has been verified. (ii) For below-cloud scavenging of aerosol species,
237 the scavenging rates have been updated to more accurately reflect the particle size dependency as described by
238 Croft et al. (2009). This update includes adjustments to the below-cloud scavenging parameters, which describe
239 the efficiency with which aerosols are removed by rain and snow, depending on the species and the assumed size
240 distribution. Additionally, a below-cloud scavenging model has been implemented.

241

242

2.2 Setup of model simulations

244 The IFS-COMPO simulations used for evaluating the impact of IFS-COMPO atmospheric composition upgrades
245 proposed for Cy49r1 on tropospheric composition, precursor gases, particle distributions and wet deposition
246 terms employ both the IFS cycles Cy48r1 and Cy49r1. Here, Cy49r1 denotes the IFS-COMPO Cy48r1 including
247 updates of aerosol/chemistry modules which are now applied in IFS Cy49r1. The meteorological component is

the same between simulations and corresponds to Cy48r1. The simulations presented here are for the year 2018, with a one-month spin-up period. The vertical resolution uses 137 individual model levels and a horizontal resolution of T$_L$511, corresponding to approx. 0.4° x 0.4° (with further details being given at https://confluence.ecmwf.int/display/UDOC/L137+model+level+definitions). The experiments do not include the data assimilation of observations, meaning that although the changes shown will not be directly visible in the final operational forecast they will influence the resulting skill scores for e.g. PM2.5. Meteorology is initialised every 24 hours based on ERA5 reanalysis data, i.e. IFS-COMPO is run in a cyclic forecast mode. A 15 minute chemical time-step is used for solving a modified version of CB05 tropospheric chemistry (Williams et al., 2022), excluding active stratospheric chemistry for efficiency (with this study being focused on changes at the surface). Three-hourly 3D global output is used for the analysis and aggregated into weekly, monthly and annual mean values.

The details of the sensitivity experiments are summarised in Table 1. The Cy48r1 reference simulation pertains to the 48R1 version of IFS-COMPO while the Cy49r1 simulation is based on the version described in Rémy et al (2024). The Cy49r1_NOEQ4C simulation is identical to the Cy49r1 simulation, except the EQSAM4Clim module (Metzger et al., 2024) is deactivated. For future reference, the experiment identities on the ECMWF Multiversion Asynchronous Replicated Storage system (MARS) are hylm (Cy48r1), i3bw (Cy49r1_NOE4C) and i3ad (Cy49r1). These three simulations use a configuration similar to those simulations presented in Remy et al. (2024) for evaluating PM.

Table 1 : Definitions of the IFS-COMPO simulations used in this study. The experiment ID's can be used to retrieve the original data from the MARS archiving system hosted at ECMWF.

Simulation	Experiment ID	Comments
Cy48r1	rd.hylm	Reference Cy48r1 model version
Cy49r1_NOEQ4C	rd.i3bw	As Cy48r1 but with all composition modeling updates for Cy49r1, except EQSAM4Clim.
Cy49r1	rd.i3ad	As Cy48r1, but with all composition modeling updates for Cy49r1, particularly activating EQSAM4Clim in both aerosols and cloud droplets

The emissions adopted in these configurations are taken from CAMS_GLOB_ANT v5.3 (Soulie et al., 2024), with biogenic emissions taken from the CAMS_GLOB_BIO v3.1 dataset (Sindelarova et al., 2022; http://eccad.aeris-data.fr/) and biomass burning emissions taken from GFAS v1.2 (Kaiser et al., 2012), all applied using the methodology as described in Ye et al. (2021), provided at 0.1 x 0.1 resolution on a monthly basis. Apart from Biomass Burning (BB) and SO$_2$, emissions are applied in the lowest model level. Volcanic outgassing of SO$_2$ is also included. Currently the emission of Di-Methyl Sulphide (DMS) is taken from a climatology, i.e. not coupled to sea surface temperature which controls biogenic activity (Deschaseaux et al., 2019). Moreover, direct production of SO$_4^=$ and HNO$_3$ in hot shipping exhausts is not accounted for (e.g. von Glasow et al., 2003).

3 Observations

For SO$_2$(g)/SO$_4^{2-}$, NH$_3$(g)/NH$_4^+$ and HNO$_3$(g)/NO$_3^-$ evaluation in Europe we compare model output against data from the EMEP measurement network as stored on the EBAS data archive (EMEP, Torseth et al., 2012; https://ebas.nilu.no/; last access 6 June 2025) using a composite of 49 individual stations located in 10 different countries, as shown in the top panel of Fig A1 in the Appendix. The sampling locations are mostly in Northern and Eastern Europe, but co-location of model output means the comparison is still valid. For the US we compare against model output aggregated on a weekly basis as derived from the in-situ measurements provided at locations included in the Clean Air Status and Trends Network (CASTNET; https://www.epa.gov/castnet, last access: 6 June 2025) using a composite of 92 individual stations distributed across the U. S., whose locations are shown in the middle panel of Fig. A1 in the Appendix. For NH$_3$(g) not direct measurements are available from the CASTNET database, therefore we compare against both weekly and yearly mean values as derived from the in-situ measurements taken from sites near CASTNET station locations (0.5 degrees radius) i.e. 92 of the current 106

348 sites in the Ammonia Monitoring Network (AMoN, https://nadp.slh.wisc.edu/networks/ammonia-monitoring-
349 network/ , last access on 6 June 2025), with measurements being at the location of CASTNET sites. No filtering
350 has been applied to these measurements due to the quality control adopted from the provider. These sites are
351 distributed more evenly across the continent. Unfortunately for S. E. Asia measurements of both precursors and
352 SIA at a weekly time frequency are not available which does not allow the same analysis for this region.

353 For evaluating the SIA particle concentrations in we use available data from the EMEP (Europe), CASTNET (US)
354 and the Acid Deposition Monitoring Network in East Asia (EANET, https://www.eanet.asia/ , last access: 6 June
355 2025; S. E. Asia) networks for SO_4^{2-}, NH_4^+ and NO_3^-. The EANET network includes 41 individual stations
356 covering a wide region, whose location is shown in the bottom panel of Fig A1 in the Appendix. Although we use
357 all of the observations provided in each database, the distribution is non-homogeneous with those in EMEP being
358 clustered towards Northern Europe and those in South-East Asia spanning a large area from Eastern China to
359 Japan. The locations of the stations used for evaluation are shown on the corresponding figures associated with
360 regional and spatial validation.

361 For the wet deposition totals we use data from the same measurement networks as those for the gaseous precursors,
362 thus removing any differences potentially introduced by spatial sampling which would potentially complicate the
363 comparisons discussed here. Specifically, these are: the EMEP network for Europe, the CASTNET network for
364 the US data and the EANET for South-East Asia. No filtering of the data was performed before making the
365 comparisons. Although seasonal variability is of interest, the EANET wet deposition totals are only provided as
366 annual mean values placing constraints on the sampling frequency used for the analysis. The averaging period
367 chosen for the evaluation is predominantly constrained by the frequency and availability of the data from South-
368 East Asia, which only provides annual mean values. For Europe and the U.S. data is provided on weekly intervals
369 (EMEP, CASTNET).

370 All statistical metrics represent spatio-temporal averages unless otherwise noted, combining all station-time
371 pairings into a single evaluation vector per region and species.

372 **4 The influence of pH on SIA chemical precursors and particulates**

373 The efficacy of SIA formation is strongly governed by the resident concentrations of the gaseous precursors.
374 Therefore changes imposed with respect to the parameterizations used for the simulating particle formation also
375 have an associated feedback effect on the precursors, due to changes in the fractional uptake governed by the solute
376 pH. In this section, we evaluate the temporal and regional distribution and biases of the both gaseous precursors
377 (SO_2, NH_3, HNO_3) and SIA (namely $SO_4^=$, NH_4^+, NO_3^-) simulated by IFS-COMPO for Europe, the U.S. and Asia.
378 Mixing ratios and particle concentrations are strongly influenced by the description and distribution of the primary
379 emission sources, meteorology, the deposition component, aerosol pH (for NH_x and NO_x) and atmospheric
380 transport. To investigate the ability of IFS-COMPO towards capturing the observed distributions we show both
381 weekly and annual mean comparisons for Cy48r1 and Cy49r1 as compared against the corresponding measurement
382 composites. In that the differences between Cy48r1 and Cy49r1_NOE4C are much smaller as shown in the budget
383 analysis of the gaseous precursors, for brevity we limit the selection of results shown. A direct link exists between
384 [NH_4^+] and [NO_3^-] in that fine mode nitrate takes the form NH_4NO_3. All observational data is used for the
385 calculation of the statistics thus they are representative of the mean across different chemical regimes. In that the
386 location of the sampling sites is not homogenous throughout the analysis region, meaning that result can be
387 weighted towards certain states/countries. For Mean Bias (MB) and Root Mean Square Error (RMSE), negative
388 percentage differences are indicative of improvements in the bias statistics, whereas for Pearson's R it is a positive
389 percentage difference.

390 To investigate the scale of such feedbacks we show monthly mean regional differences for July and December
391 2018 for the three selected regions below focusing on the gaseous distributions of SO_2, NH_3 and HNO_3. For
392 evaluating the performance of IFS-COMPO we aggregate at a weekly frequency. For the corresponding
393 distributions and concentrations of SIA we show annual mean values against observations.

394

395

396 **4.1 SO_2 and $SO_4^=$**

429 Figure 1 shows the regional monthly mean distributions in surface SO₂ mixing ratios for July and December 2018
430 for Cy48r1, along with the percentage differences between Cy48r1, Cy49r1_NOEQ4C and Cy49r1. When
431 comparing the spatial distributions across regions, Europe exhibits the lowest SO₂ mixing ratios in Cy48r1, where
432 the region has undergone strong mitigation practices over the last decades (e.g. Vestreng et al, 2007). The maps
433 for December show higher mixing ratios towards the East, with a significant contribution from shipping. For the
434 US, a stark East-West gradient exists as governed by the continental distribution in anthropogenic emissions, with
435 higher emissions towards the East Coast, again with a seasonal signature. Maximal surface mixing ratios are 5-
436 10 times higher than those simulated for Europe distributed over a much larger area. As expected, China exhibits
437 the highest mixing ratios of between 10-20 ppb over the entire country, which is approximately 20 times higher
438 than those simulated for Europe for both months shown.

439 When comparing Cy48r1 against Cy49r1_NOE4C there are reductions in [SO₂(g)] at the surface for all regions
440 of between 0-10%, resulting in limited increases in SO₄²⁻ production of a few percent due to changes other than
441 those related to updates to aerosol and solution pH. This small increase in the SO₄²⁻ production is reversed when
442 applying the EQSAM4Clim pH methodology (Metzger et al., 2024), where the conversion efficacy of SO₂ is
443 faster at a more alkalinic pH. The global budget terms show that in addition to primary emission, approximately
444 one third of SO₂ in the troposphere, comes from the oxidation of DMS by the hydroxyl radical (OH), with DMS
445 originating from biogenic activity in the oceans.

446 In Cy48r1, approximately 20% of SO₂ is oxidised in the gas-phase and 43% in the aqueous phase, with the
447 remaining 37% being lost to surface via dry and wet deposition. This increase in gas-phase production via OH is
448 linked to changes imposed by differences in O₃-NOₓ reaction cycles near anthropogenic source regions which
449 results in a small increase in O₃ of a few percent (not shown). The corresponding values for Cy49r1_NOE4C
450 show changes in the order of a few percent across terms, increasing the global burden by 1.5% mostly in the lower
451 troposphere. For Cy49r1 the application of EQSAM4Clim pH in cloud droplets reduces both the uptake and
452 oxidation of SO₂ by reducing aquated sulphite ([SO₃²⁻]ₐq, pKa(HSO₃⁻)=7.2) and an enhancement of the gas-phase
453 oxidation due to increased OH, resulting in more gas-phase production of H₂SO₄ which is subsequently scavenged
454 into solution further increasing solution acidity (lower pH values) in case of excess SO₄²⁻ (insufficient cations to
455 completely neutralise all SO₄²⁻).

Figure 1			

458 shows that the region with the highest surface SO₂ is the North-East of the U.S., with the other regions moderating
459 the biases. Again little seasonality exists in the weekly observational composites. There is a positive bias for
460 wintertime and a negative bias for summertime around 0.5-1.0 μg/m³ across all simulations. There is an increase
461 in the annual mean negative bias by around 0.1 μg/m³ in Cy49r1 with poor correlation with the observations.
462 Finally for China, weekly SO₂ concentrations are an order of magnitude larger than those observed in the other
463 regions reaching 15-20 μg/m³ during wintertime. The simulated concentrations exhibit a very large positive bias
464 of between 10-20 μg/m³, suggesting that the regional SO₂ emissions are likely overestimated in the global
465 inventory. Only a negligible improvement occurs in Cy49r1 where no detectable correlation exists between the
466 simulated and observed values.

467 Figure 2 shows a comparison of weekly [SO₂(g)] and [SO₄²⁻] surface composites as simulated in IFS-COMPO
468 against weekly composites of measurements taken from the EMEP measurement network (top left panel). For
469 SO₂(g) a consistent positive bias exists for the entire year across all IFS-COMPO simulations suggesting emission
470 estimates which are high, where surface concentrations exhibit around 100% positive bias, increasing to almost
471 200% during wintertime. The variability in the observational means (grey shaded area) does indicate that the
472 simulated increase in surface [SO₂(g)] during wintertime does occur at some of the measurement sites. The
473 corresponding observational means of [SO₄²⁻] show that there is higher weekly variability during wintertime than
474 summertime, with concentrations ranging typically between 1.0-2.0 μg/m³. This significant weekly variability is
475 simulated well by IFS-COMPO across all simulations. For wintertime both Cy48r1 and Cy49r1 exhibit significant
476 positive biases of 0.5-1.0 μg/m³. Surprisingly, Cy49r1_NOE4C has the lowest bias during wintertime of around

Moved down [1]: Due to the primary source term of SO₂ being direct emissions indicates that estimates for Eastern Europe could be too high (c.f.

Moved down [2]: The annual mean bias (MB) value decreases by around 25%, with a moderate correlation. For the US the weekly mean SO₂ values in the observations are typically around 2.5 μg/m³, which is more than double that observed in Europe.

Deleted: Figure 1 shows weekly comparisons of surface SO₂(g) concentrations (μg/m³) from the three different regions for 2018 against observational composites assembled using data from background/rural stations as selected from the relevant observational networks introduced in Sect. [...] [1]

Deleted: Fig1A in the Appendix).

Deleted: ¶
Figure A1 in the Appendix details...the regional monthly mean distributions in surface SO₂ mixing ratios for July and December 2018 for CY48R1...y48r1, along with the [...] [2]

Formatted: Font: 10 pt

Deleted: CY48R1...y48r1 against CY49R1 [...] [3]

Deleted: CY48R1...y48r1, approximately 20% of SO₂ is oxidised in the gas-phase and 43% in the aqueous phase, with the remaining 37% being lost to surface via dry and wet deposition. This increase in gas-phase production via O[...] [4]

Deleted: Table 2 : The annual Mean Bias (MB), Root-Mean Square Error (RMSE) and Pearsons R values for the comparisons of the weekly mean regional distributions and concentrations of gaseous SO₂ as compared against [...] [5]

Moved down [3]: Wet Deposition

Deleted: Figure 1A...shows that the region with the highest surface SO₂ is the North-East of the U.S., with the other regions moderating the biases. Again little seasonality exists in the weekly observational composites. There is a posi[...] [6]
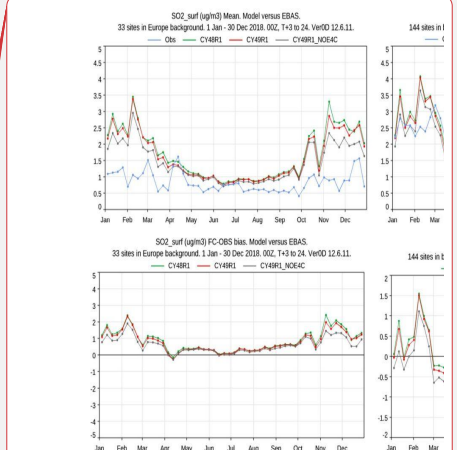
Deleted: [...] [7]

Formatted: Right

727 0.2-0.5 µg/m³. Comparing Cy49r1 against Cy48r1 shows an increase in surface $[SO_4^{2-}]$ by approximately 10-25%
728 during wintertime in Cy49r1, albeit still with a significant negative bias of around 0.8-1.5 µg/m³. During
729 summertime the weekly variability in the observed weekly means is much lower with monthly gradients being
730 captured well in IFS-COMPO. All simulations capture the extent of this variability quite well. Differences across
731 simulations is around 0.1-0.2 µg/m³, with Cy49r1 having a slightly higher bias. Due to the primary source term
732 of SO_2 being direct emissions indicates that estimates for Eastern Europe could be too high (c.f. Fig. 1). The
733 annual mean bias (MB) value decreases by around 25%, with a moderate correlation. For the US the weekly mean
734 SO_2 values in the observations are typically around 2.5 µg/m³, which is more than double that observed in Europe.
735 For 2018 there is generally a low annual MB in Cy48r1 (-0.41 µg/m³), which is subsequently reduced in
736 Cy49r1_NOE4C (-0.20 µg/m³) and Cy49r1 (+0.01 µg/m³). The correlation coefficient also shows a marginal
737 improvement from 0.37 (Cy48r1/Cy49r1_NOE4C) to 0.43 (Cy49r1).

Moved (insertion) [1]
Moved (insertion) [4]
Moved (insertion) [2]
Deleted: the winter months. There
Deleted: CY48R1
Deleted: CY49R1
Deleted: CY49R1
Deleted: CY48R1/CY49R1
Deleted: CY49R1).
Formatted: Font: Times New Roman, 10 pt

Formatted: Right

744
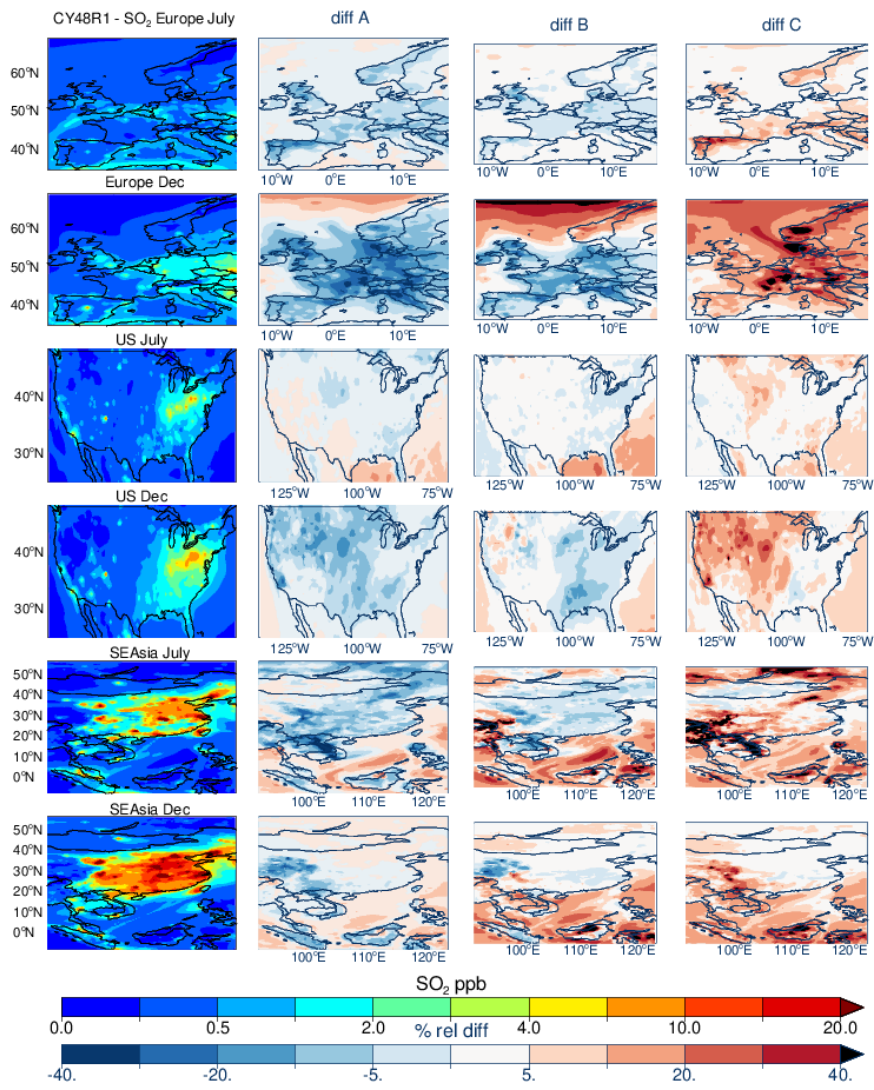
Figure 1: The horizontal monthly mean distribution for surface SO$_2$ for Cy48r1 for July and December 2018 for Europe (top), the United States (middle) and South-East Asia (bottom). The corresponding relative differences when compared against the other simulations. Panel definitions : Diff A=(Cy49r1_NOEQ4C - Cy48r1)/Cy48r1; Diff B=(Cy49r1-Cy48r1)/Cy48r1 and Diff C=(Cy49r1-Cy49r1_NOEQ4C)/Cy48r1.

Table 2 The tropospheric SO$_2$ budget in Tg S/year for 2018 as calculated by Cy48r1, Cy49r1_NOE4C and Cy49r1, with the associated percentage differences being provided in parentheses as e.g. ((Cy49r1-Cy48r1)/Cy48r1)*100.

Process	Cy48r1	Cy49r1_NOE4C	Cy49r1

Emission	54.0	54.0 (-)	54.0 (-)
DMS + OH → SO_2	21.8	21.8 (-)	21.5 (-1.6)
SO_2 + OH → H_2SO_4	15.1	15.4 (+2.3)	16.5 (+9.3)
SO_2 (aq) →SO_4 (aq)	33.7	33.9 (+1.2)	33.0 (-2.2)
Dry Deposition	21.6	21.3 (-3.0)	22.2 (+3.0)
Wet Deposition	8.2	8.0 (-3.0)	6.9 (-15.8)
Burden	0.70	0.71 (+1.4)	0.75 (+7.1)
Lifetime (days)	3.25	3.29 (+1.2)	3.48 (+7.1)

751

752

Figure 2: A comparison of weekly mean SO_2 and SO_4^{2-} for Europe (left panels; µg/m³) and the US (right panels) simulated in IFS-COMPO as compared against EMEP and CASTNET observational networks, respectively, for 2018. The sampling frequency of the data for SEAsia does not allow a corresponding weekly plot for this region.

In the right hand panels of Fig. 2 a similar comparison is made against weekly observational composites of surface [$SO_2(g)$] and [SO_4^{2-}] from the CASTNET measurement network. Similar to Europe, no seasonal cycle exists in the observations of either surface [$SO_2(g)$] and [SO_4^{2-}] with typical weekly mean values of around 0.7-1.0 µg/m³, even though the latitudinal range is large for the CASTNET measurement stations. For the wintertime lower weekly MB occur for both Cy49r1_NOE4C and Cy49r1 as compared with Cy48r1, where the weekly variability is inverse of that seen in the observations. During the summertime much larger positive biases occur reaching between 200-300% across all IFS-COMPO simulations which exhibit a strong seasonal cycle in spite of no such increase in the simulated [$SO_2(g)$]. Although some smaller differences occur between simulations, there is no improvement in Cy49r1 with respect to the weekly MB. Considering the corresponding high summertime MB for SO_2 shows either a significant fraction is transported in IFS-COMPO, where a slower oxidation rate of SO_2 by OH and/or aqueous phase processing would be required to improve the performance of IFS-COMPO which would then lower the negative bias seen for [$SO_2(g)$].

Figure 3 shows the annual means of surface [$SO_2(g)$] and [SO_4^{2-}] for Cy48r1 and Cy49r1 for Europe and the US. The changes in surface [SO_4^{2-}] here are somewhat unaffected by the changes in aerosol pH due to EQSAM4Clim that are shown in Rémy et al. (2024) for 2019 due to the dominant aqueous-phase production term (albeit with small increases due to the additional contribution from organic acids). One main difference for SO_x than either NH_x or NO_x, is that the gas-particle partitioning is dependent on cloud pH, dissolved O_3 and hydrogen peroxide (H_2O_2), where SO_4^{2-} production is irreversible.

For Europe the sampling sites for this aerosol species in the EMEP network are located such that comparisons for southern european countries are not included in the regional mean statistics or discussed further. A sharp North-South gradient exists imposed by the variability in H_2SO_4 production between seasons, cloud cover for the wet production term and the distribution of the primary point sources for SO_2 emissions, although mitigation measures remove the increase in the emitted flux during the cold winter months associated with domestic heating (Versteeg et al., 2007). Simulated concentrations in Cy48r1 are lower in Scandinavia as compared with e.g. France, which results in a low bias of around 1 µg/m³ in e.g. Finland and around the Baltic, here related to missing shipping emissions of SO_2, which quickly converts to SO_4^2 in the plume (Celik, et al., 2020) . For the other sites in Europe agreement is better with the low bias decreasing to approx. 0.5 µg/m³. One outlier exists for the most easterly station, which exhibits a significant high bias of 1.5 µg/m³. Comparing Cy49r1 shows increases in the simulated surface [SO_4^{2-}] of between 0.2-0.4 µg/m³, which leads to an improved bias. Only small improvements are made to the correlation coefficient due to identical emission estimates being used and EQSAM4Clim affecting SO_x the least, i.e., only indirectly through changes in pH.

For the U.S. the CASTNET observations show an East-West continental gradient in surface [SO_4^{2-}] exists as determined by the distribution in the primary SO_2 emissions and transport (c.f. Figure 1). A significant transport component exists for SO_4^{2-}, resulting in surface [SO_4^{2-}] in the Marine Boundary Layer between 1.0-2.5 µg/m³, where transport dominates local surface [SO_4^{2-}] produced from DMS oxidation (Simpson et al., 2014). For Cy49r1 there is a reduction in surface [SO_4^{2-}] at continental scale, with a decrease in the annual MB from 0.67 to 0.20 µg/m³, with a corresponding increase in the correlation coefficient to 0.43, albeit remaining only rather weakly correlated. For the West of the U.S. a positive MB is introduced for the rural background in Cy49r1 of 0.5-0.7 µg/m³, with a contribution being transported from the East. Hence, reductions in the annual MB primarily stem from improved agreement at Eastern U.S. monitoring sites. That a positive MB of approx. 1-1.5 µg/m³ exists in the annual mean values around Kentucky/Tennessee suggests that the local SO_2 emission estimates are too high (see Discussion in Sect. 5).

For South-East Asia, the scarcity of sampling sites in the EANET network results in a less robust evaluation. Also many sampling sites are located at coasts rather than inland, thus the influence of changes at coastal regions have a large influence on the regional statistics. Higher primary SO_2 emissions occur on the land. Therefore any positive MB near source regions are not included in the statistics; the results shown here for surface SO_4^{2-} should be considered lower limits. The long-range transport of SO_4^{2-} in Asia has been shown to somewhat neutralise national SO_2 mitigation measures taken in e.g. Taiwan and South Korea. This originates from changing trends in SO_2 emission from mainland China as captured by EANET measurement sites (Chang et al, 2022). For Cy48r1 the annual mean statistics show a very low MB and a good correlation coefficient of 0.75. For Cy49r1 there is a significant degradation, where the MB increases to 0.48 µg/m³ showing a trend in the performance for SO_x that is similar to the U.S. . Notably, the more remote sampling stations (e.g. oceanic) exhibit regional negative biases (approx. -0.7 µg/m³) whereas those situated near Mongolia and South Korea agree well with low MB values. For Thailand and Vietnam there are typically large MB values, suggesting regional SO_2 emission estimates are too high. Unfortunately there are no in-situ measurements available for better quantification. The correlation coefficient degrades in Cy49r1 compared to Cy48r1 towards 0.66. Overall, the improvements are mixed for the SO_2 - SO_4^{2-} couple and much less pronounced compared to the other SIA.

954

Figure 3 : Comparisons of annual mean [SO$_4$$^{2-}$] simulated at the surface in Cy48r1 and Cy49r1 when compared
against measurements for the three selected regions during 2018 (µg/m^3). The corresponding regional statistics
are provided in Table 3. The site locations used are shown in each pane and taken from the EMEP, CASTNET
and EANET networks respectively.

959

960

961

962

Formatted: Right

Table 3 : The annual MB, RMSE and Pearsons R values for the comparisons of the daily (EMEP, Europe), weekly (CASTNET, US) and annual (EANET, South-East Asia) mean regional distributions and concentrations of surface SO_4^{2-} as compared against composites assembled from the observations for 2018 shown in Fig. 4 for Europe, the US and South-East Asia. Percentage differences are calculated as ((Cy49r1-Cy48r1)/Cy48r1)*100 and given in parentheses.

$SO_4^=$	Europe (EMEP)		US (CASTNET)		SE Asia (EANET)	
	Cy48r1	Cy49r1	Cy48r1	Cy49r1	Cy48r1	Cy49r1
MB ($\mu g/m^3$)	-0.49	-0.32 (-35)	0.67	0.20 (-70)	-0.02	0.48 (+96)
RMSE	1.35	1.31 (-3)	0.93	0.46 (-50)	1.64	2.28 (+39)
Pearsons R	0.45	0.47 (+4)	0.33	0.43 (+23)	0.75	0.66 (-12)

4.2 NH$_3$ and NH$_4^+$

The regional distribution of surface NH$_3$ for 2018 in the three chosen regions and the resulting changes which occur due to both the IFS cycle upgrades and the application of EQSAM4Clim are shown in Figure 4. Although there is a declining trend in European regional NH$_3$ emissions (Tichý et al, 2023), a strong seasonal cycle exists in Cy48r1. Maximal mixing ratios are situated around Benelux and Northern Italy, with local differences of 8-20 ppb between July and December across regions. The CAMS_GLOB_ANT v5.3 (Soulie et al, 2024) emission inventory has recently been validated for NH$_3$ against top-down estimates providing confidence in the quality of the estimates for Europe (Ding et al., 2024). For the US a similar seasonal signature exists especially for the North West and South East associated with agricultural emissions (Wang et al, 2020), with background mixing ratios of between 0.5-2.0 ppb remaining relatively constant. For China, whose NH$_3$ emissions have increased over the last decades (Liu et al., 2019; Chen et al. 2023), surface mixing ratios of between 5-20 ppb occur for July for large areas, again associated with agricultural practices. Likewise, high mixing ratios are found around Bangladesh (> 20 ppb). For December, mixing ratios are typically an order of magnitude lower, with the exception of the South-West, which again exhibits high mixing ratios (> 20 ppb). Measurements of NH$_x$ over the ocean are rare, thus the large increase shown cannot be verified. Nevertheless, estimates range from 0.1-4.2 ppb depending on season and location (Sharma et al., 2012) indicating that Cy48r1 has a significant negative bias which is somewhat improved in Cy49r1.

Figure 5 shows comparisons between weekly observational composites from EMEP of [NH$_3$(g)] against those extracted from the various IFS-COMPO simulations for 2018. The observational composite shows that there is a skewed seasonal cycle exhibiting a maxima in April/May from agricultural activity, with wintertime values being around 0.5 $\mu g/m^3$ increasing to 0.8-1.5 $\mu g/m^3$ during spring and summertime. This seasonal variability is captured across all simulations. For wintertime there is a low weekly bias of around 0.1$\mu g/m^3$ and a positive summertime weekly bias of between 0.5-2 $\mu g/m^3$ in Cy48r1 (annual MB 1.04 $\mu g/m^3$), where a 20% increase in the bias is simulated for Cy49r1 (annual MB 1.21 $\mu g/m^3$). There is a high correlation across simulations resulting in values from 0.71-0.73, where the occurrence of weekly increases in the observed values are typically captured in IFS-COMPO.

The bottom left panel of Fig. 5 shows that there is a reversed seasonality in [NH$_4^+$] in the observational means, with higher [NH$_4^+$] during wintertime due to the colder temperatures decreasing the volatility of the particles (e.g. Tang et al., 2021). Moreover, for Cy48r1 there is clearly a large positive bias of [NH$_4^+$] with little change in Cy49r1_NOE4C. Table 4 provides the global budget terms for all three simulations, showing the large increase in deposition terms and tropospheric burden for NH$_3$(g). For Cy49r1, the improved gas/particle partitioning from EQSAM4Clim reduces the particle phase concentrations of the semi-volatile aerosol species which leads to an increase in the respective gas phase concentrations, also affecting aerosol pH. This determines the solubility of NH$_3$(g), also contributing to its reduced conversion into NH$_4^+$ (see Table 4, approx. 44% reduction), which is an effect amplified by the inclusion of mineral cations (i.e. Ca^{2+}, Na$^+$, K$^+$, Mg^{2+}). The tropospheric lifetime of NH$_3$(g) more than doubles in Cy49r1 allowing more transport from strong source regions, in line with changes in the tropospheric burden. Both the associated loss due to dry and wet deposition increases (37% and 51%, respectively), due to lower NH$_4^+$ particle production (see Sect. 4.2).

1063

Figure 4: As for Fig. 1 except for NH₃. Panel definitions : Diff A=(Cy49r1_NOEQ4C - Cy48r1)/Cy48r1; Diff B=(Cy49r1-Cy48r1)/Cy48r1 and Diff C=(Cy49r1-Cy49r1_NOEQ4C)/Cy48r1.

Therefore, there is a modest degradation in performance as compared with Cy48r1. Comparing Cy48r1 and Cy49r1_NOE4C shows that there are typically decreases of [NH₃(g)] of between 5-20% over the land across the chosen regions, as a result of the changes to wet scavenging in the absence of decrease in pH (reducing 13% and increasing the burden by 20% c.f. Table 4).

1070 **Table 4**. The tropospheric NH_3 budget in Tg N/year for 2018 as calculated by Cy48r1, Cy49r1_NOE4C and
1071 Cy49r1, with the associated percentage differences being provided in parentheses as e.g. ((Cy49r1-
1072 Cy48r1)/Cy48r1)*100.

Process	Cy48r1	Cy49r1_NOE4C	Cy49r1
Emission	51.1	51.1 (-)	51.1 (-)
$NH_3 + OH$	0.82	0.99 (+20)	1.98 (+240)
$NH_3 \rightarrow NH_4^{\pm}$	30.6	30.3 (-1)	17.3 (-44)
Dry Deposition	16.3	16.6 (+2)	22.4 (+37)
Wet Deposition	7.0	6.2 (-13)	10.6 (+51)
Burden	0.13	0.16 (+19)	0.29 (+118)
Lifetime (days)	0.9	1.1 (+22.0)	2.0 (+133)

1073

1074
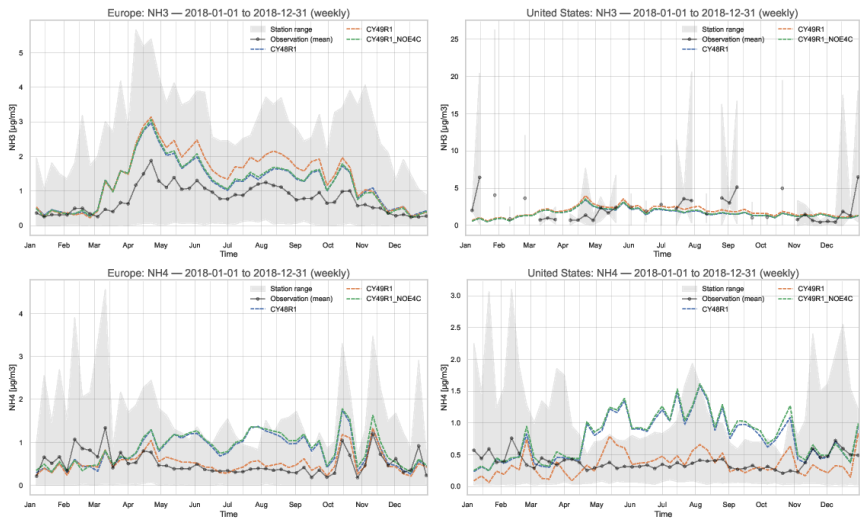
1075 **Figure 5:** A comparison of weekly mean [$NH_3(g)$] and [NH_4^+] at the surface for Europe (left panels; µg/m³) and the
1076 US (right panels) as simulated in IFS-COMPO as compared against the composites of measurements taken from
1077 EMEP and CASTNET for 2018. For the U.S. the data for $NH_3(g)$ is taken from the AMoN measurement network.
1078 The data frequency provided for the South-East Asia region does not allow a corresponding plot, although annual
1079 statistics are provided in Table 5.

1080 Also shown in Fig. 5 are weekly comparisons of observational composites of [NH_4^+] at the surface from the EMEP
1081 measurement network against those extracted from the various IFS-COMPO simulations for 2018 (bottom left panel).
1082 Although the maximum observed $NH_3(g)$ shown in the top panel of Figure 5 occurs during April/May, higher [NH_4^+]
1083 are observed during the winter months. For both Cy48r1 and Cy49r1_NOE4C summertime mean biases of > 100%
1084 exist (0.5 µg/m³) which are removed by the application of EQSAM4Clim in Cy49r1 resulting in a very low bias < 0.1
1085 µg/m³. This potentially improves the accuracy of forecasting both PM2.5 and PM10 significantly by reducing the
1086 cumulative bias across aerosol types (where the definition of both aggregate quantities are given in Rémy et al., 2024).

Deleted: Figure 4
Deleted: EBAS archive
Deleted: .
Deleted: 4
Deleted: CY48R1
Deleted: CY49R1
Deleted: CY49R1
Formatted: Right

1094 Similar comparisons are shown in Fig. 5 for the US in the bottom right panel using weekly composites assembled
1095 from the CASTNET data in the bottom right panel. In contrast to the seasonal cycle for [NH$_3$(g)], which peaks during
1096 April/May, the corresponding seasonal cycle in the weekly [NH$_4^+$] values peaks during July, being fairly consistent
1097 between 1.5-1.75 μg/m^3 during summertime. This indicates that a saturation occurs with respect to NH$_4^+$ particle
1098 formation which is most likely linked to availability of HNO$_3$(g) (c.f. See sect 4.3. below). Again significant biases
1099 exist in Cy48r1 and Cy49r1_NOE4C, reaching around 1.5 μg/m^3 during summertime (which is 600% of the
1100 summertime observational values). Applying EQSAM4Clim halves this positive bias in Cy49r1, resulting in fairly
1101 good agreement during the winter and summer months.

1102 **Table 5** : As for Table 3 except for NH$_4^+$.

	Europe (EMEP)		US (CASTNET)		SE Asia (EANET)	
NH$_4^\pm$	Cy48r1	Cy49r1	Cy48r1	Cy49r1	Cy48r1	Cy49r1
MB (μg/m^3)	0.26	-0.05 (-81)	0.95	0.23 (-48)	0.96	0.55 (-43)
RMSE	0.94	0.72 (-23)	1.71	0.46 (-73)	1.73	1.30 (-25)
Pearsons R	0.46	0.62 (+29)	0.59	0.43 (-27)	0.59	0.44 (-25)

1103

1104 Figure 6 shows the distribution of the corresponding annual mean [NH$_4^+$] for the three chosen regions for both Cy48r1
1105 and Cy49r1 during 2018, with the associated regional annual mean statistics being given in Table 5. The location of
1106 the measurement sites are shown in each panel, with the respective annual mean values within each circle. Significant
1107 decreases in the conversion rate of NH$_3$ in Cy49r1 results in lower [NH$_4^+$]. This is a result of the improved gas/aerosol
1108 partitioning and the subsequent increase in aerosol pH when applying EQSAM4Clim (see Table 4; Rémy et al., 2024).
1109 More direct depositional loss to the surface for NH$_3$(g) occurs in Cy49r1 due to increased residence time. There is a
1110 wide variability in the simulated aerosol pH between regions, with Europe exhibiting aerosol pH values of around 3-
1111 4, whereas the Southern U.S. and Northern China exhibit aerosol pH values in the range 2-3 (Pan et al, 2024; Rémy
1112 et al, 2024) which indirectly affects the temporal variability in NH$_4^+$ production. Once formed, regional transport
1113 contributes to the continental distribution of NH$_4^+$ away from strong source regions (e.g. Simpson et al., 2010; Renner
1114 and Wolke, 2010; Du et al, 2020).

1115 For Europe (top panels), most observational annual mean values are between 0.2-1.2 μg/m^3 which are exceeded by >
1116 50% in Cy48r1. In Cy49r1 the reductions in the annual mean [NH$_4^+$] are of the order of 0.5-1.0 μg/m^3 and result in
1117 low annual mean [NH$_4^+$] values for e.g. Spain/UK, whilst reducing maximal concentrations by approx. 50% in
1118 Northern Italy. This subsequently contributes to a reduction in the cumulative PM2.5 biases for this region as shown
1119 in Rémy et al. (2024) for 2019. The associated MB values in Table 5 show a significant reduction in the bias (> 80%)
1120 along with an increase in the correlation coefficient, although the simulated NH$_4^+$ distribution is still only moderately
1121 correlated (*r*=0.62). Unfortunately, the lack of available measurements means no quantification of the performance
1122 of IFS-COMPO around the mediterranean can be shown. It should be noted that with a more realistic distribution and
1123 seasonal variability in NH$_3$(g) emissions (e.g. Shepard et al, 2011; Dammers et al, 2019), the [NH$_4^+$] distributions
1124 shown here will most likely not be affected as other SIA species determine the NH$_3$ – NH$_4^+$ gas/aerosol partitioning.

1125 For the U.S. (middle panels) similar decreases in annual mean [NH$_4^+$] values occur in Cy49r1 as compared to Cy48r1,
1126 with very low concentrations of between 0.1-0.4 μg/m^3 for the West of the U.S., which shows less bias when compared
1127 against the observational mean values. This causes a reduction in the annual mean regional bias of around 0.7 μg/m^3
1128 as shown in Table 5. A gradient exists in the aerosol pH from EQSAM4Clim ranging from annual mean values of
1129 pH=3.0 towards the North-West U. S. and becoming more acidic towards the South West U.S. with annual mean
1130 values of pH=2.0 (Rémy et al., 2024). This reduces the transfer of NH$_3$(g), thus moderating NH$_4^+$ production (c.f.
1131 Table 5). For the North-East U.S. with high NO$_x$ emissions, there are reductions of between 0.5-1.0 μg/m^3. For the
1132 South-West U.S., with high [NH$_3$(g)] from agriculture (c.f. Fig. 5) there are reductions of between 0.3-1.0 μg/m^3.
1133 There is a degradation in the correlation coefficient exhibiting a moderate annual mean correlation with significant
1134 overestimates for the South-West U.S. as shown for the comparisons of [NH$_3$(g)] at selected sites in Figure 5.

Deleted: Figure A5 in the Appendix

Deleted: .

Deleted: as shown in Fig A4

Deleted: Fig A7 in the Appendix; Sect next subsection).

Deleted: CY48R1

Deleted: CY49R1

Deleted: 25

Deleted: CY49R1

Deleted: A comparison of the weekly variability in [NH$_3$]$_g$ between IFS-COMPO and measurements from a selection of rural sites which contribute to the AMON measurement network for 2018 is shown in Figure A5 in the Appendix, with the details of each site being provided in the figure legend and sites chosen to cover a wide area of the US. In general, the measurements indicate that wintertime [NH$_3$(g)] are lower than summertime concentrations across multiple sites, except in California which experiences less seasonal variability in temperature (and agricultural practices). Maximal concentrations are in the range of 1-6 μg/m^3 occurring during either springtime (Alabama / New York) or summertime (Florida) depending on the extent and timing of agricultural activity in each respective state. In general differences between CY48R1 and CY49R1_NOE4C are negligible, whereas the weekly bias is significantly reduced for CY49R1. An exception is Arizona where the large positive bias indicates a too high local emission flux. The incidence of high [NH$_3$(g)] in CY49R1 is also somewhat dependent on the local [HNO$_3$(g)] via NO$_x$, which is the other important precursor with respect to [NH$_4$(NO$_3$)] (contrast New York State versus Alabama). The seasonality derived from the weekly variability is captured to a large degree, with the amplitude of the cycle being substantially improved in CY49R1.¶   ... [15]

Deleted: CY48R1

Deleted: CY49R1

Deleted: 6

Deleted: also

Deleted: CY49R1

Deleted: CY49R1

Deleted: CY48R1

Deleted: CY49R1

Deleted: 6

Deleted: (see Discussion).

Deleted: CY49R1

Deleted: CY49R1

Deleted: 6

Deleted: 4

Deleted: Figure A2

Deleted:)+]

Deleted: 6

1223
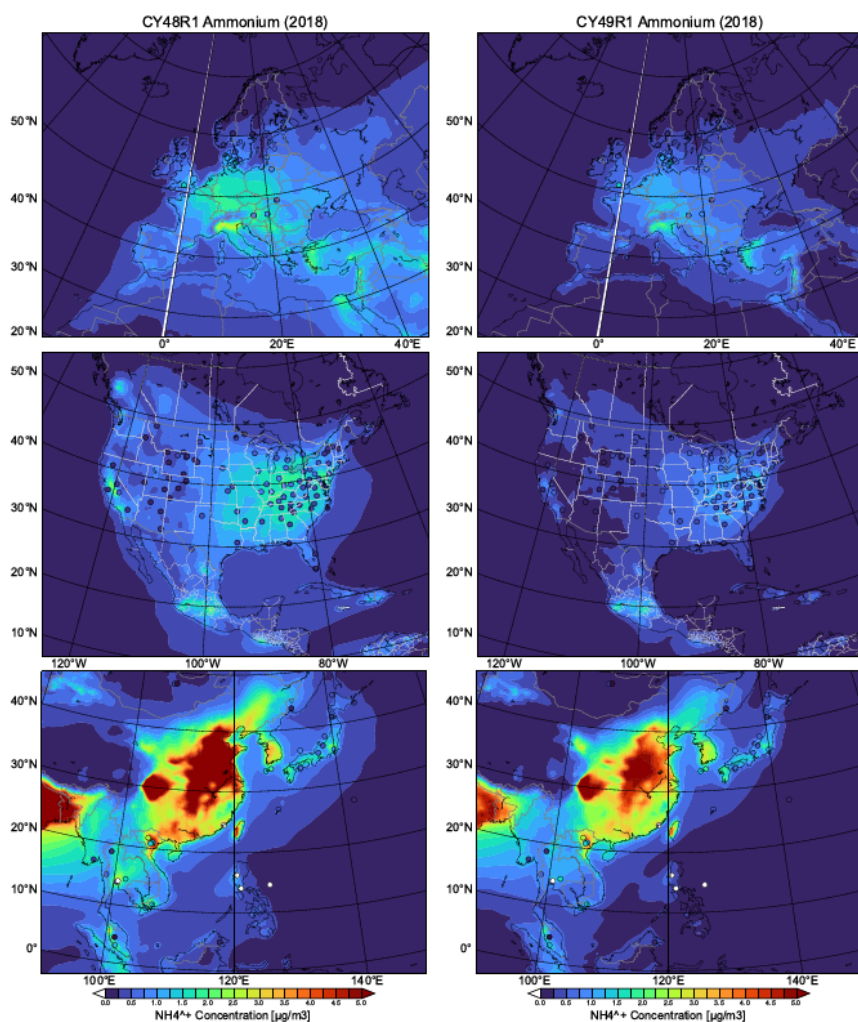
Figure 6 : Comparisons of annual mean [NH$_4^+$] simulated at the surface in Cy48r1 and Cy49r1 when compared against measurements for the three selected regions during 2018 (µg/m^3). The corresponding regional statistics are provided in Table 5. The site locations used are shown in each pane and taken from the EMEP, CASTNET and EANET networks respectively.

For South-East Asia (bottom panels), the simulated annual mean [NH$_4^+$] over land are typically much higher than those simulated for either Europe or the U.S., with maximal values of between 7.0-9.0 µg/m^3 for Eastern China, in-spite of the similar surface mixing ratios in NH$_3$(g) between Europe and China as shown in Fig. 5. This difference is predominantly driven by the relatively high HNO$_3$(g) in China due to the more polluted chemical regime (the availability of O$_3$(g), NO$_2$(g) and OH(g) determining gas-phase HNO$_3$(g) production). Applying EQSAM4Clim in Cy49r1 results in significant decreases of between 1-2 µg/m^3 [NH$_4^+$] as associated with the highest annual mean [NH$_4^+$] > 6.0 µg/m^3. This reduces the associated annual mean regional bias by 0.4 µg/m^3, with a corresponding reduction in the correlation, due to less transport. Again the lack of sampling sites in the region with high primary

NH₃(g) emissions skews the associated annual mean biases. For the more remote locations (e.g. Mongolia/South China Sea) low values of < 0.5 µg/m³ are captured well in both Cy48r1 and Cy49r1.

4.3 HNO₃ and NO₃⁻

Figure 7 shows the monthly mean regional distribution of HNO₃(g) for July and December 2018 for the three chosen regions for Cy48r1, along with the relative differences when compared with Cy49r1_NOE4C and Cy49r1. The corresponding global chemical budget terms for HNO₃(g) are provided in Table 6. No direct emission of HNO₃ occurs in IFS-COMPO, which is often prescribed in global chemistry transport models to represent e.g chemistry in the plumes of ships (e.g. Vinken et al., 2011), with the main source being the oxidation of NO₂ by OH in the gas-phase as shown in Table 6. This production term increases in Cy49r1 by approx. 14% as a result of the enhancements in OH via changes in O₃ (not shown). For heterogeneous conversion, the cumulative HNO₃ production term is approx 50% that of the gas-phase production term, remaining relatively constant between simulations. There is a shift between fine mode NO₃⁻ (NH₄NO₃) and coarse mode NO₃⁻ (CaNO₃/NaNO₃), strengthening the link between NH₄⁺ and NO₃⁻ in IFS-COMPO. Both dry and wet loss terms increase significantly due to the increase in the availability of HNO₃(g), which reduces the fraction converted to NO₃⁻. The temporal variability of HNO₃(g) is influenced by the magnitude and extent of regional NOₓ emissions, photochemical activity (via OH formation), gas/aerosol partitioning (where particles with high SO₄⁻ content having an associated low NO₃⁻ content) and scavenging in clouds and aerosols.

For Europe very low surface mixing ratios occur over land for both months shown in Cy48r1 (< 0.1 ppb), which is surprising considering that the Benelux has been shown to have high NOₓ levels (van der A, 2024) therefore likely to have correspondingly high HNO₃(g) mixing ratios. Higher mixing ratios of between 0.25-0.5 ppb occur around the Coasts and the Mediterranean originating from direct shipping emissions of NO₂. This can lead to elevated NO₃⁻ concentration due to uptake of HNO₃(g) on sea salt, which might be too high as the current formulation of EQSAM4Clim only assumes thermodynamic equilibrium which is not dynamically limited. A coupling with a dynamical aerosol model is foreseen. In contrast, the application of EQSAM4Clim in Cy49r1 results in large increases in surface HNO₃(g) at continental scale during July. For December, a strong latitudinal variability in the relative differences imposed in Cy49r1 occurs, with decreases of between 25-75% in HNO₃(g) at latitudes higher than 60°N due to lower temperatures and lower RH under a relatively low NOₓ environment.

For the U.S., the highest HNO₃(g) mixing ratios in Cy48r1 occur for the Eastern states and California (1-2 ppb), with much lower values in the more remote Central U.S. (0.1-0.2 ppb), with a strong seasonal cycle in maximal values peaking in July. Comparing relative differences between simulations shows a significant increase of surface HNO₃(g) in Cy49r1 (between 0.1-6 ppb) at continental scale for both months, with the largest increases occurring in the Northern States. In contrast to Europe no seasonal decreases occur for any location.

Finally for South-East Asia, the surface mixing ratios are the highest across all regions, with maximal values being of the order of 4-5 ppb towards the Eastern Coast (July) and Central regions (December). Comparing the relative differences between simulations shows significant increases of between 50-5000%, with the exception of the more remote regions to the North. As for Europe, a strong seasonality can be seen with decreases above 30°N occurring regardless of the NOₓ regime. As shown for NH₃ (c.f. Fig. 4), there are significant increases in HNO₃ over the ocean for both months shown, associated with lower [NO₃⁻] (as shown by the cumulative reduction in global conversion by 50%).

Figure 7: As for Fig. 1 except for HNO₃. Panel definitions : Diff A = (Cy49r1_NOEQ4C - Cy48r1)/Cy48r1; Diff B = (Cy49r1-Cy48r1)/Cy48r1 and Diff C = (Cy49r1-Cy49r1_NOEQ4C)/Cy48r1.

Figure 8 shows the resulting changes in surface [HNO₃(g)] across simulations for Europe when compared against weekly composites assembled from EMEP measurement sites (top left panel). The location of these sites is shown in Figure A1 in the Appendix, where the location of the sampling sites results in a significant bias in the evaluation towards Northern Europe. No obvious seasonal cycle is evident in the observational weekly means, with concentrations in the range of 0.3-0.7 μg/m³, although many sites are located away from strong NOₓ sources. Both Cy48r1 and Cy49r1_NOE4C exhibit negative weekly biases resulting in under-estimations of around 100% during the summertime, although the weekly variability is captured to a degree. There is a reduction in the bias of around 0.1 μg/m³ in Cy49r1_NOE4C showing that the other changes made between IFS cycles cause changes in the gas-phase production term in addition to the changes in NH₄NO₃ from EQSAM4Clim (c.f. Table 8). For Cy49r1 there
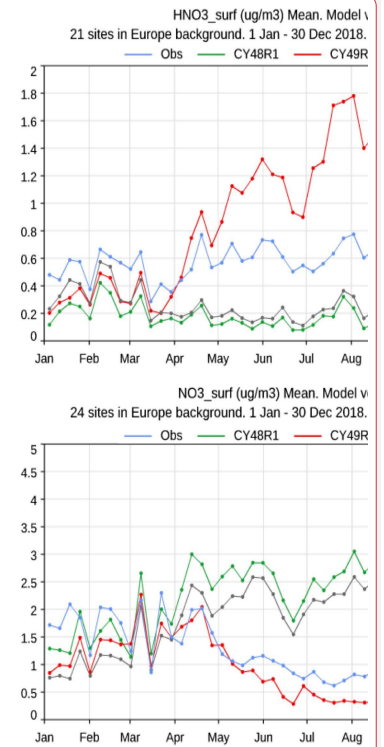
Deleted: **6** : A comparison of weekly mean [

Deleted: (g)]

Deleted: [NO₃⁻] for Europe (μg/m³) at the

Deleted: as simulated in CY48R1 (green), CY49R1_NOE4C (grey) and CY49R1 (red) as

Deleted: measurement

Deleted: stations representative of a background scenario for 2018. The evolution in the corresponding bias values are also

Deleted: the bottom panel

is a significant excess of [HNO$_3$(g)] due to enhanced production and less transfer into the particulate phase, in spite of an increase in the cumulative deposition terms. Such changes are associated with relatively low [HNO$_3$(g)] IFS-COMPO values of around < 0.1 ppb.

Table 6: The tropospheric HNO$_3$ budget in Tg N/year for 2018 as calculated by Cy48r1, Cy49r1_NOE4C and Cy49r1, with the associated percentage differences being provided in parentheses as e.g. ((Cy49r1-Cy48r1)/Cy48r1)*100.

Process	Cy48r1	Cy49r1_NOEQ4Clim	Cy49r1
NO$_2$ + OH → HNO$_3$	11.0	11.6 (+5)	12.6 (+14)
N$_2$O$_5$ + Liq → HNO$_3$	2.2	2.5 (+12)	2.6 (+17)
N$_2$O$_5$ + Aer → HNO$_3$	3.2	2.3 (-28)	2.3 (-27)
NO$_3$ + Aer → HNO$_3$	0.8	0.4 (-47)	0.5 (-42)
HNO$_3$ → Fine NO$_3$-	1.4	1.2 (-18)	2.0 (+41)
HNO$_3$ → Coarse NO$_3$-	9.3	5.9 (-36)	3.6 (-61)
Dry Deposition	2.0	2.4 (+17)	5.1 (+150)
Wet Deposition	6.8	5.9 (-13)	9.3 (+38)
Trop. Burden	0.31	0.30 (-3)	0.32 (+3)

Figure 8 also shows comparisons of weekly [HNO$_3$(g)] from the CASTNET measurement network in the US are shown in the top right panel. As for Europe both the concentrations and seasonal variability in the observations is low, with typical weekly concentrations being around $\pm$0.5 µg/m^3. The rather equal distribution of measurement sites in the US means the evaluation presented does not have any significant regional bias. That the measured weekly mean concentrations are rather constant is surprising considering that variability in the gas-phase chemical production term involves OH, which has strong seasonality from the differences in day length. In contrast to Europe, both Cy48r1 and Cy49r1_NOE4C show good agreement against the measurements with weekly biases of the order of 0.2-0.25 µg/m^3. However, for Cy49r1 a large positive bias is introduced by the use of EQSAM4Clim due to a limitation in the ability for HNO$_3$ to condense on particle surfaces, such that condensed HNO$_3$ does not contribute to NH$_4$NO$_3$ formation (which requires a coupling of EQSAM4Clim with an aerosol dynamical model as e.g., described in Metzger et al., 2018). It also shows that although the cumulative global dry and wet deposition terms in Cy49r1 have increased markedly compared to Cy48r1 (c.f. Table 6), which is insufficient to compensate for the reduced aerosol formation.

The bottom left panel of Figure 8 shows the corresponding changes in surface [NO$_3$-] as shown for HNO$_3$ for Europe. The observational composites show that [NO$_3$-] is almost twice that of the corresponding [HNO$_3$(g)] during wintertime, with similar concentrations during summertime. Unlike for HNO$_3$(g), a shallow concave seasonal cycle exists in the weekly observational composites, related to seasonal differences in temperatures and lifetime (Tang et al., 2021). Both Cy48r1 and Cy49r1_NOE4C fail to capture the correct seasonality and exhibit higher concentrations during summertime, resulting in substantial positive biases of 1-2 µg/m^3. Considering the associated biases in [HNO$_3$(g)] shows that the HNO$_3$-NO$_3$- partitioning is not captured well. For Cy49r1 the description of the seasonal cycle is significantly improved due to the inclusion of EQSAM4Clim, resulting in much lower biases of < 0.5 µg/m^3 throughout the year, also pointing to the importance of a better representation of gas/particle partitioning. The right bottom panel of Fig. 8 shows the corresponding changes in [NO$_3$-] against weekly composites from the CASTNET measurement network. A similar seasonal cycle exists as for Europe with similar concentrations. For Cy48r1 and Cy49r1_NOE4C an inverse seasonal variability occurs in [NO$_3$-] as compared with the observational weekly means, resulting in significant positive biases of around 1.0-1.5 µg/m^3. For Cy49r1 biases decrease by an order of magnitude and the seasonal variability is improved markedly, again showing improved particle distribution when using EQSAM4Clim.

1414

Figure 8 : A comparison of weekly mean [HNO₃(g)] and [NO₃⁻] for Europe (left panels; μg/m³) and the US (right panels) at the surface as simulated in IFS-COMPO as compared against measurement composites from EBAS (left) and CASTNET (right) stations for 2018. The various simulations are defined within the panels and the grey band represents the variability in the measurement values across stations.

In Figure 9 we show the corresponding regional distributions of the annual mean [NO₃⁻] for Cy48r1 and Cy49r1 during 2018 for the three chosen regions, where the associated changes in the regional annual mean statistics are provided in Table 7. Some commonality exists between the changes shown for annual mean [NH₄⁺] and annual mean [NO₃⁻], due to the speciation of the SIA involved. The cumulative sums of the smaller nitrate particle (fine mode NO₃⁻ in Table 6 with the form NH₄(NO₃)) and the larger nitrate particle (coarse mode NO₃⁻ in Table 6 with the form of CaNO₃ and NaNO₃) are both included in the plots. Therefore the changes evaluated here are a combination of changes to both the fine and coarse mode NO₃⁻, rather than the changes associated with individual particle sizes. In contrast to the reduced N analysis provided above, which is impacted more directly due to changes in the fine mode NO₃⁻, the [NO₃⁻] is also indirectly affected by the coarse mode assumptions through the effect of cations on the neutralisation level that subsequently controls the gas/aerosol equilibrium partitioning. The change in the partitioning for HNO₃ shown above results in an associated reduction in the fraction of NOₓ held in particulate form due to e.g. a higher dry deposition component.

For Europe, the simulated annual mean [NO₃⁻] in Cy48r1 generally ranges between 0.2-2.0 μg/m³ over Scandinavia/Spain and the surrounding seas and between 2.0-6.3 μg/m³ over North-Western/Central Europe and the Mediterranean, becoming lower towards the North-East and South-West. The highest European NOₓ emissions occur around the South-East of the UK, Benelux, the Ruhr and Po valleys (e.g. Liu et al., 2021; van der A., 2024). This, and the rather homogeneous distribution within Central Europe shows that a significant degree of transport occurs once NO₃⁻ particles are formed. No such continental gradient in the annual mean [NO₃⁻] exists in the observational mean values indicating an overestimate in IFS-COMPO. Nevertheless, in Cy49r1 decreases of [NO₃⁻

1448] of between 2-4 µg/m³ occur for the Baltic states/France/Germany and over the Mediterranean Sea (from
1449 relatively high shipping NOₓ emissions) compared to Cy48r1. This results in much better
1450 agreement with the annual mean observed values for the individual measurement
1451 stations. The annual regional MB is reduced by ≅ 90%, decreasing to 0.1 µg/m³ in
1452 Cy49r1 with an associated increase in the correlation coefficient due to lower transport of [NO₃⁻] out of the main
1453 source region. A large impact occurs due to the acidification of sea salt aerosols under relatively high NOₓ emission
1454 from dense shipping lanes, which can be seen by similar [NO₃⁻] reductions over the sea, though difficult to evaluate
1455 due to the lack of sufficient measurements.

1456
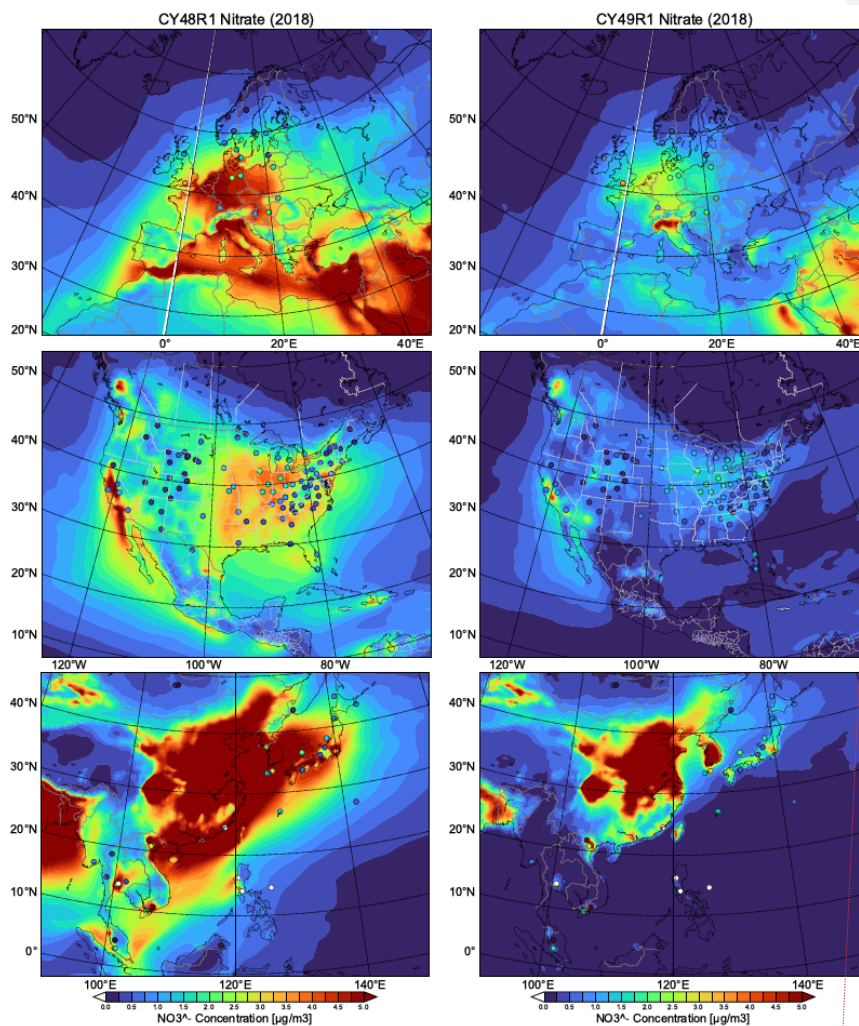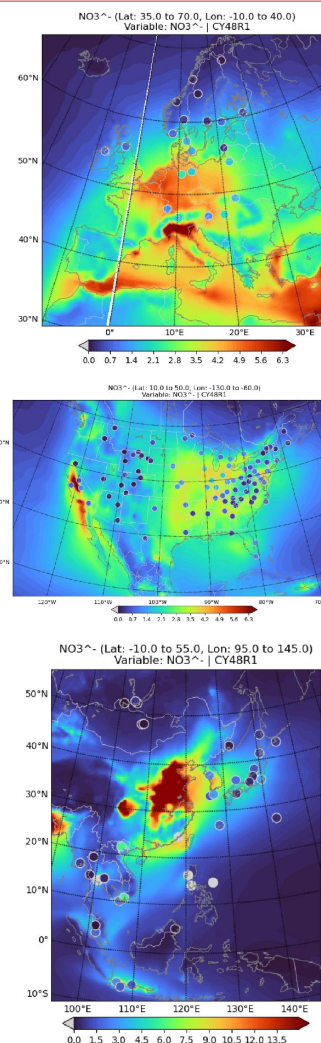
1457 **Figure 9:** Comparisons surface comparisons of [NO₃⁻] simulated in Cy48r1 and Cy49r1 as compared against
1458 measurements for the three selected regions given in µg/m³. The corresponding regional statistics are provided in

Table 7. The site locations used are shown in each pane and taken from the EMEP, CASTNET and EANET networks respectively.

For the U.S., there is a similar impact on [NO$_3^-$] as shown for Europe, where the high annual MB in [NO$_3^-$] decreases significantly (94%) from Cy48r1 to Cy49r1. For Cy48r1, [NO$_3^-$] typically ranges between 2-4 µg/m^3 with medium-range transport resulting in appreciable concentrations over the surrounding oceans. Considering the precursors, there is surprisingly little variability in the observed annual mean [NO$_3^-$] despite the large difference in the resident [HNO$_3$(g)] across different states of the U.S. related to the distribution of the NO$_x$ emissions (Figure 7; Goldberg et al., 2021). Only in the southwest, around California, the annual mean [NO$_3^-$] > 2.0 µg/m^3, shows typical annual mean [NO$_3^-$] being ≤ 1.0 µg/m^3 in Cy49r1 for the majority of the U.S. This implies that the cations used as input for EQSAM4Clim imposes a limit concerning the phase-transfer of HNO$_3$(g) into more acidic aerosols via neutralisation of the anions by cations in the particle phase.

Table 7 : As for Table 3 except for NO$_3^-$.

	Europe (EMEP)		US (CASTNET)		SE Asia (EANET)	
NO$_3^-$	Cy48r1	Cy49r1	Cy48r1	Cy49r1	Cy48r1	Cy49r1
MB (µg/m^3)	0.95	0.10 (-90)	1.71	0.10 (-94)	2.68	-0.16 (-94)
RMSE	2.37	1.60 (-32)	2.20	0.83 (-62)	3.62	1.41 (-61)
Pearsons R	0.41	0.58 (+29)	0.31	0.57 (+46)	0.65	0.52 (-20)

5 The changes in regional wet deposition

In this section, we evaluate the temporal distribution and biases associated with the annual wet deposition terms of soluble trace gas species and particulates. All three SIA are lost to the surface by both dry and wet deposition processes. Over the last decades the main source of acidification has shifted from SO$_x$ based to NO$_x$ based in line with the reduction measures imposed for SO$_x$ and the increase and associated emission changes from e.g. road transport. Here we evaluate whether the current version of IFS-COMPO captures the correct wet scavenging for the various dissolved precursors and SIA. Evaluations are made using comparisons of model output against annual wet deposition totals as taken from the observational networks introduced in Sect. 3. The concentrations of the dissolved precursors (i.e. SO$_2$(aq), NH$_3$(aq) and HNO$_3$(aq)) also undergo wet deposition (in IFS-COMPO) and cannot be differentiated well in the observational networks but are included in the measured totals. The wet deposition term is also influenced by meteorological parameters such as the simulated large-scale and convective mixing, liquid and solid precipitation droplet size, SAD, and the frequency and intensity of precipitation as provided by the IFS model.

In Table 8, the changes in the global tropospheric burden, lifetime, dry and wet deposition totals for SO$_4^{2-}$, NH$_4^+$, NO$_3^-$ (fine) and NO$_3^-$ (coarse) during 2018 across all simulations are given. The corresponding statistics for the comparison with observations for the wet deposition annual means of SO$_x$, reduced N and oxidised N are provided for the three chosen global regions in Table 9.

Table 8: The global budget values for the burden, tropospheric lifetime, wet and dry deposition terms for SO$_4^{2-}$, NH$_4^+$ and NO$_3^-$ for 2018. Totals are provided in Tg S/year and Tg N/year. Percentage difference changes are are calculated as ((Cy49r1-Cy48r1)/Cy48r1)*100 and given in parentheses.

	Cy48r1	Cy49r1 NOE4C	Cy49r1
SO$_4^{2-}$			

	Cy48r1	Cy49r1_NOE4C	Cy49r1
Burden	0.4	0.6 (+30)	0.6 (+30)
Lifetime (days)	3.4	4.4 (+29)	4.4 (+29)
Dry dep	5.8	5.4 (-7)	5.4 (-7)
Wet dep	43.1	43.9 (+2)	44.2 (+3)
NH_4^+			
Burden	0.3	0.4 (+32)	0.2 (-33)
Lifetime (days)	3.5	4.6 (+34)	4.1 (+18)
Dry dep	5.1	5.1 (-)	1.8 (-64)
Wet dep	27.5	27.1 (-2)	20.1 (-40)
NO_3^- (fine)			
Burden	0.01	0.01 (-)	0.02 (+86)
Lifetime (days)	4.9	5.4 (+12)	6.1 (+25)
Dry dep	0.2	0.2 (-21)	0.1 (-32)
Wet dep	0.6	0.5 (-13)	1.0 (+64)
NO_3^- (coarse)			
Burden	0.01	0.01 (-)	0.01 (-)
Lifetime (days)	3.4	3.8 (+11)	2.4 (-29)
Dry dep	1.5	2.5 (+73)	1.2 (-18)
Wet dep	3.5	2.8 (-20)	0.7 (-79)

1544

Table 9: The annual MB, RMSE and Pearsons R values for the comparisons of the weekly mean regional wet deposition totals of dissolved $SO_2+SO_4^-$, $NH_3+NH_4^+$ and $HNO_3+NO_3^-$ as compared against composites assembled from the regional observation networks for 2018 shown in Figures 9-11 for Europe, the U.S. and South-East Asia. Percentage difference changes are calculated as (($Cy49r1-Cy48r1$)/$Cy48r1$)*100 and given in parentheses.

	Europe (EMEP)		US (CASTNET)		SE Asia (EANET)	
SO_x	Cy48r1	Cy49r1	Cy48r1	Cy49r1	Cy48r1	Cy49r1
MB (mgS/m^2/yr)	-42	-38 (-9)	137	190 (+39)	-44.2	8.7 (-80)
RMSE	88.2	85 (-3)	203	270 (+33)	447	500.3 (+12)
Pearsons R	0.55	0.58 (+6)	0.68	0.66 (-3)	0.72	0.65 (-10)
Reduced N						
MB (mgN/m^2/yr)	61	25.9 (-58)	8.4	6.8 (-21)	12	-44 (+260)
RMSE	114	93.4 (-18)	76.0	81.3 (+7)	318	302 (-5)
Pearsons R	0.69	0.68 (-1.4)	0.77	0.72 (-16)	0.75	0.71 (-1)
Oxidised N						
MB (mgN/m^2/yr)	9.7	-1.4 (-86)	130	99.7 (-23)	142	98.3 (-31)
RMSE	69	72 (+4)	153	122.6 (-20)	324	274.3 (-15)
Pearsons R	0.50	0.47 (-6)	0.86	0.85 (-1)	0.67	0.68 (+2)

1549

Deleted: CY48R1
Deleted: CY49R1
Deleted: CY49R1
Formatted Table
Deleted: 10
Deleted: 8-10
Deleted: CY49R1-CY48R1)/CY48R1
Formatted Table
Deleted: CY48R1
Deleted: CY49R1
Deleted: CY48R1
Deleted: CY49R1
Deleted: CY48R1
Deleted: CY49R1
Formatted: Space After: 10 pt, Line spacing: single
Formatted: Right

5.1 Total annual wet S deposition

Figure 10 shows the regional distribution of annual wet S deposition for Europe, the U.S. and South-East Asia in both Cy48r1 and Cy49r1 during 2018. To allow a direct comparison across regions we use a colour scale which covers values larger than 500 mgS/m²/year in South-East Asia. The global budget terms for SO_4^{2-} are presented in Table 8 and show that, in spite of the global burden increasing by one third, only very small increases of a few percent occur in the annual wet SO_4^{2-} totals (Rémy et al., 2024). However, the significant increase in the tropospheric SO_4^{2-} lifetime means more remains in the aerosol phase will impact the degree of scattering in IFS-COMPO as shown for AOD comparisons in Remy et al. (2024). The most significant change is in the direct gas-phase production term of $H_2SO_4(g)$, where increases in $[SO_2(g)]$ subsequently increase the total mass scavenged into aqueous cloud droplets. This results in an extent of acidification (slowing in-situ oxidation; c.f. Table 2), which is somewhat buffered by the increased phase transfer of $NH_3(g)$ (c.f. Table 4). Although there is a 15% reduction in the total global $SO_2(aq)$ wet deposition, the increases in $[SO_4^{2-}(aq)]$ results in an increase in the cumulative wet S deposition annual totals.

For Europe (top panels), the changes between model simulations are similar to the changes in the $SO_2(g)$ and SO_4^{2-} particle concentrations discussed in Sect. 4 . Compared against the annual EMEP mean observational values, which range from 100-900 mgS/m²/year, there is generally an underestimation in Cy48r1 of approx. 100-150 mgS/m²/year for North-West Europe, Poland and on the Iberian Peninsular. For other regions the agreement is quite good, capturing the observed deposition gradient from Germany into Austria/Northern Italy. A limited number of measurement stations exhibit very high localised values (e.g. South-West Ireland, Palma), indicating missing primary emission sources in the global inventory. For Cy49r1, strong similarity exists for Benelux, Denmark and Italy, where negative biases of around 50-100 mgS/m²/year occur. A significant negative annual MB exists in Europe, which decreases by around 10% in Cy49r1 (c.f. Table 9) with a marginal increase in the correlation. This is impacted by the associated negative MB for $SO_2(g)$ during summertime (c.f. Figure 2) and the large values observed at selected stations influencing the regional mean.

For the U.S. (middle panels) there is a stark contrast to the changes shown for Europe. Assessing the annual mean values from CASTNET shows that an observational gradient exists in the wet deposition annual totals, similar as that for the location of primary SO_2 emission sources (c.f. Fig. 1), with maximal values reaching 300-400 mgS/m²/year towards the East Coast. For Cy48r1, this gradient is captured well albeit with large positive biases of > 100 mgS/m²/year, resulting in a maximal range of 700-900 mgS/m²/year. There is a significant annual wet deposition in the Atlantic (250-300 mgS/m²/year) due to the oxidation of DMS (released from the ocean) and the long-range transport of $SO_2(g)/SO_4^{2-}$ from the anthropogenic source regions. In Cy49r1 the area of maximal wet S deposition increases around, e.g., New York State, resulting in an increase in the positive annual MB by nearly 40% to 190 mgS/m²/year. This is in contrast to the significant improvement in the annual MB for $[SO_4^{2-}]$ given in Table 3, indicating that there is an increase in the scavenging into the aqueous phase of SO_4^{2-} particles due to the other cumulative updates of IFS-COMPO (c.f. Table 8), in part due to the 10% increase in gas-phase SO_2 to H_2SO_4 (Table 8).

Finally for South-East Asia (bottom panels), EANET annual wet depositional totals show that more than twice the amount of S deposition occurs as measured in either Europe or the U.S. over an identical timeframe, reaching 1200-1300 mgS/m²/year in Central China and Indonesia. The spatial distribution of stations shows that a positive gradient exists between deposition totals in China and those extending towards Indonesia (2000-2200 mgS/m²/year; not shown). This indicates the importance of the transport component of SO_4^{2-} when considering the low regional $SO_2(g)$ precursor mixing ratios around the equator (c.f. Fig. 1), and that the primary sources are typically infrequent volcanic eruptions for the region between 5°N-5°S (Fioletov et al., 2020) that typically inject the SO_2 above the boundary layer (thus with a limited impact on the surface values).

Towards the Coast of Eastern China the observations show annual totals of 250-350 mgS/m²/year, in contrast to high values near the middle of China. This is surprising, considering that high SO_2 emissions are defined in IFS-COMPO around South Korea rather than Central China. The implication is that the regional SO_2 emissions employed for this region are likely too high, considering the low regional deposition values. The regional annual MB improves markedly to 8.7 mgS/m²/year, which is very low considering the high values in the measurements. This is accompanied by a degradation in the correlation coefficient from 0.72 to 0.65.
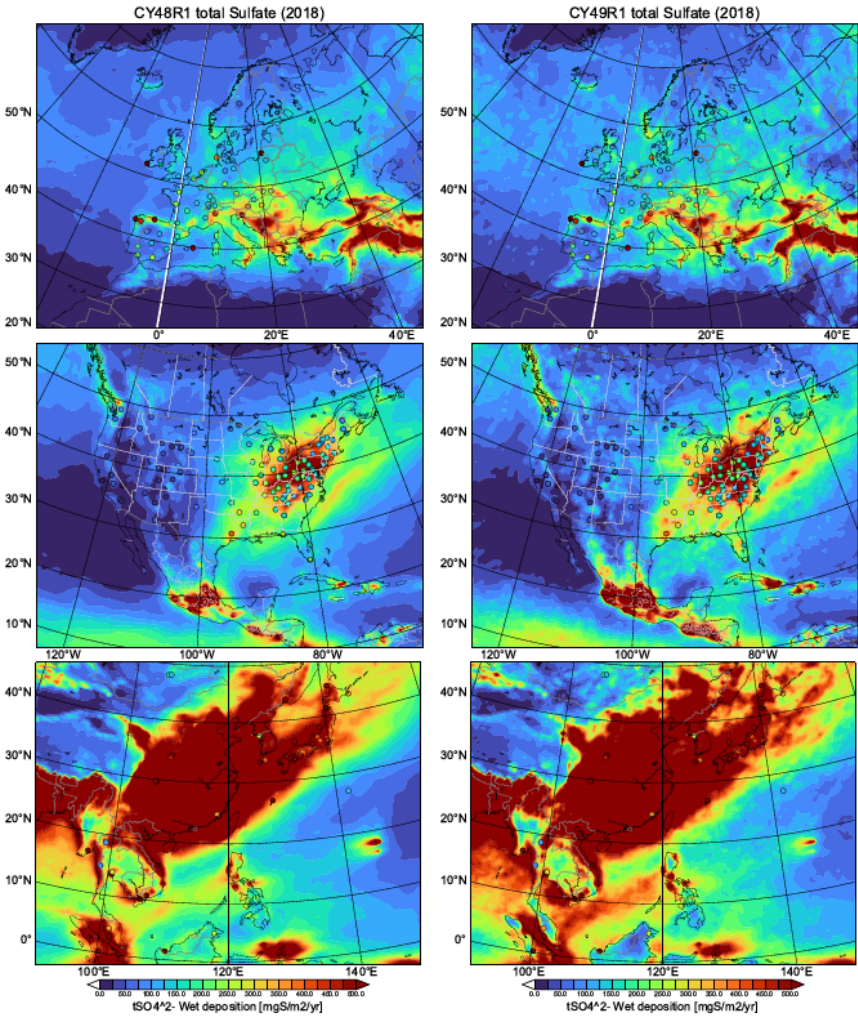
Figure 10 : Annual comparisons of the cumulative wet deposition totals of dissolved SO_2 and SO_4^{2-} aerosol (mgS/m²/year) for 2018 as simulated in Cy48r1 (left column) and Cy49r1 (right column) shown for Europe (top), the U.S. (middle) and SE Asia (bottom). The corresponding statistics are provided in Table 9. The site locations used are shown in each pane and taken from the EMEP, CASTNET and EANET networks respectively.

5.2 Total annual wet NHₓ deposition

In Figure 11 we show the corresponding changes in the total annual mean wet deposition of reduced N for both Cy48r1 and Cy49r1 during 2018. The location of the sampling stations is identical to those shown above for the wet S deposition evaluation. In Table 8, the global chemical budget terms for NH_4^+ show that the cumulative updates to IFS-COMPO increase the tropospheric burden by one third (similar to SO_4^{2-}, with $(NH_4)_2SO_4$ being a dominant SIA, Seinfeld and Pandis, 2006), which is subsequently reversed when applying EQSAM4Clim for the description of aerosol and cloud pH, as seen when comparing Cy48r1 and Cy49r1. This results in significant decreases in both the total annual global dry and wet deposition terms, as illustrated for the three select regions (> 50% from Table 8).

For Europe (top panels), where high summertime $NH_3(g)$ mixing ratios are simulated (c.f. Figure 6 in Sect. 4), the EMEP observational annual wet deposition totals show that peak values exist in the Balkans and Northern Italy (Po valley), and that local regional variability exists in e.g. France (ranging between 250-350 mgN/m²/year). For regions with low NH_3 emissions, such as Scandinavia and the Iberian Peninsula, wet deposition totals have a lower range, of between 50-200 mgN/m²/year. For Cy48r1, the high resident surface mixing ratios of $NH_3(g)$ (5-15 ppb) results in a relatively high NHₓ annual total wet deposition values of between 350-500 mgN/m²/year for North-West and Central Europe at a country-wide scale (e.g. Benelux, Austria). Measured annual mean values are typically exceeded, which results in an annual MB of 61 mgN/m²/year, albeit with a high correlation of 0.69 (c.f. Table 8). The continental distribution is therefore represented well, although high values extend too far to both the East and West of Europe. Comparing the annual mean temporal distribution simulated in Cy49r1 shows a reduction in the area with maximal values (> 450 mgN/m²/year). The reduction in $[NH_4^+]$ (c.f. Table 4) reduces the annual MB in wet deposition by nearly 60% , without any notable degradation in the correlation coefficient. Thus, the application of EQSAM4Clim significantly improves the simulation of reduced N wet deposition in IFS-COMPO for Europe.

For the U. S. (middle panels), the AMoN observations show that there is a similar East-West gradient in the total reduced N wet deposition totals as that for $NH_3(g)$ surface mixing ratios and $[NH_4^+]$ distributions. The range in observed total wet deposition values is between 30-400 mgN/m²/year showing that, in the absence of local NH_3 sources, that levels of deposition are rather low (lower than that observed for Europe). Comparing the temporal distribution of reduced N wet deposition in Cy48r1 shows that the continental gradient is captured, although maximal values which occur towards Iowa are not seen in the measurements (>100% MB) being influenced by the high local NH_3 emission flux. For the East-Coast, where most primary NH_3 sources are located, there is generally an overestimation in the wet deposition simulated in Cy48r1. Compared to Europe, the annual MB for the U. S. is low at 9 mgN/m²/year. This low annual MB is a result of a large positive bias towards the East that is moderated by underestimates in other parts of the U.S. . However, a high degree of correlation (R=0.72) is achieved for Cy49r1. Although the spatial distribution of NH_4^+ is similar between model cycles, the reduction in $[NH_4^+]$ results in associated reduction of 21% in the annual MB and a slight degradation in the correlation coefficient.

For South-East Asia, the EANET observational annual mean wet deposition totals show that much higher values occur than for the other two regions presented. Similar to that shown for wet S, values range between 200-2400 mgN/m²/year (not shown), with the highest measured values in Indonesia and Vietnam. The simulated temporal distribution in wet reduced N deposition does capture the variability across individual strations quite well across a wide area. In Cy48r1, the annual MB is 12 mgN/m²/year on high annual totals resulting in it being the lowest for all the regions, with a high correlation coefficient of 0.75. For Cy49r1, there is a larger negative MB (although still relatively small compared to the large totals), in-spite of the lower (positive) MB simulated for the $[NH_4^+]$ comparisons as compared to Cy48r1 (c.f. Table 5).

Formatted: Font: 10 pt
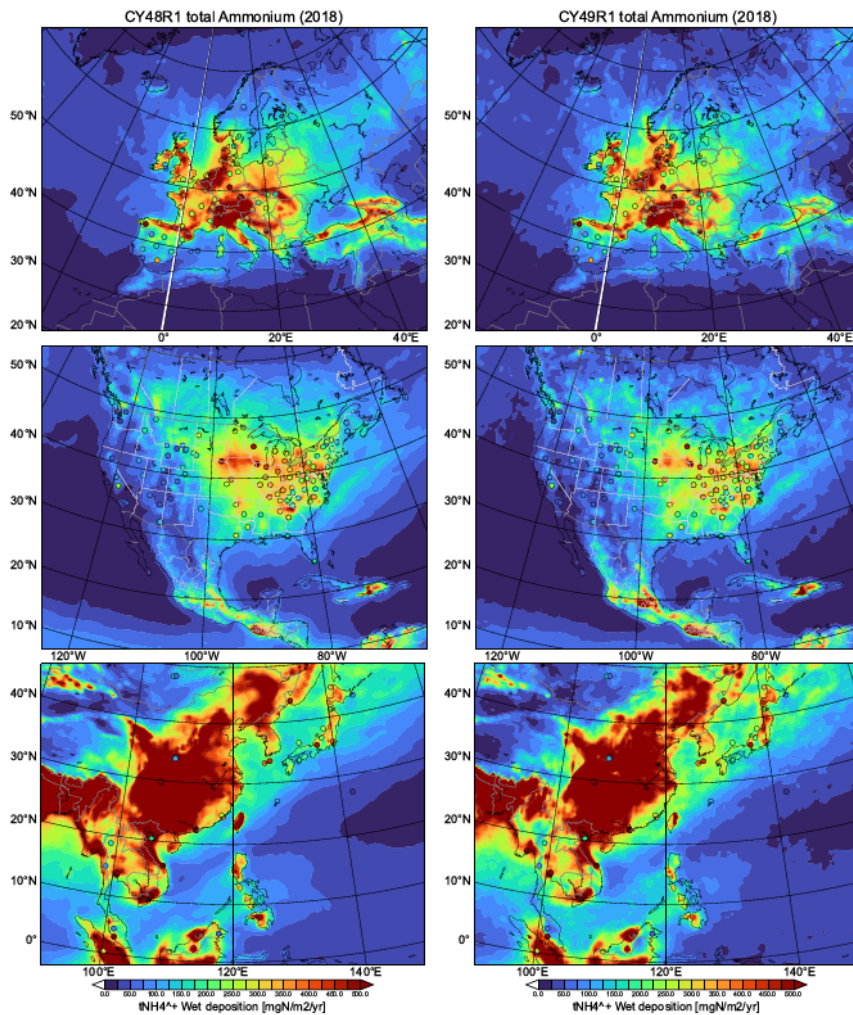
Figure 11 : Annual comparisons of the cumulative wet deposition totals of dissolved NH_3 and NH_4^+ aerosol (mgN/m²/year) for 2018 as simulated in Cy48r1 (left column) and Cy49r1 (right column) shown for Europe (top), the U.S. (middle) and SE Asia (bottom). The corresponding statistics are provided in Table 9. The site locations used are shown in each pane and taken from the EMEP, CASTNET and EANET networks respectively.
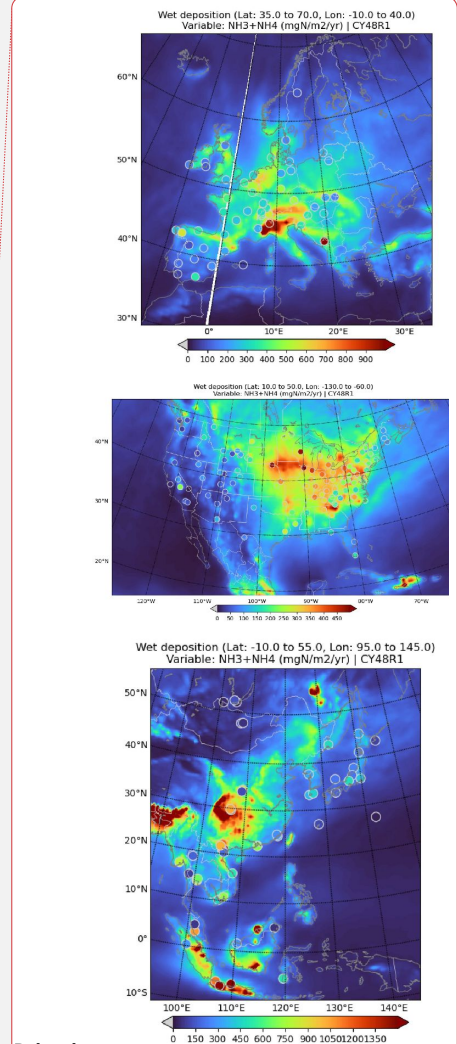
Deleted:

Deleted: 9

Formatted: Indent: Left: 0 cm, Right: 0,03 cm

Deleted: CY48R1

Deleted: CY49R1

Formatted: Right

1738   **5.3 Total annual wet NOx deposition**
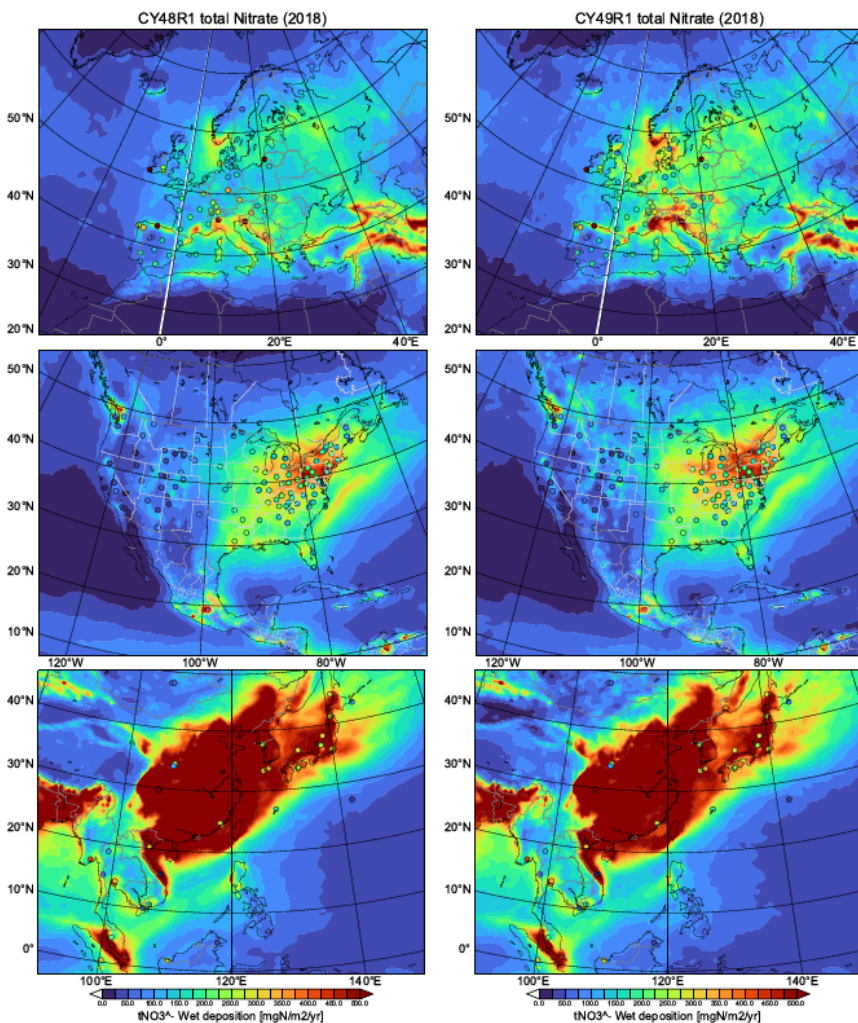
1739
1740   **Figure 12 :** Annual comparisons of the cumulative wet deposition totals of dissolved HNO_3 and NO_3^- aerosol
1741   (mgN/m^2/year) for 2018 as simulated in Cy48r1 (left column) and Cy49r1 (right column) shown for Europe (top),
1742   the U.S. (middle) and SE Asia (bottom). The corresponding statistics are provided in Table 9.The site locations
1743   used are shown in each pane and taken from the EMEP, CASTNET and EANET networks respectively.

1744   Finally, in Figure 12 we show the corresponding changes in the total annual mean wet deposition of oxidised N
1745   for both Cy48r1 and Cy49r1 during 2018. The global chemical budget terms provided in Table 6 shows that there
1746   is an increase in the gas-phase production term for HNO_3, with a relatively constant heterogeneous conversion
1747   term for N_2O_5 when summed over the various reactive surfaces. Once formed, a significant fraction of HNO_3 is
1748   directly scavenged into aqueous cloud droplets and deposited to the surface as wet (acidic) deposition (c.f. Rémy
1749   et al, 2024). However, the large biases shown for HNO_3(g) does reveal a limit to the wet scavenging term with an

Deleted: 10

Deleted: CY48R1

Deleted: CY49R1

Deleted: 7

Formatted: Right

2939

excess remaining in the gas phase, which impacts the results shown in this section. Note that the particulate NO_3^- takes various chemical forms in IFS-COMPO ($Ca(NO_3)_2$, $NaNO_3$, KNO_3, NH_4NO_3), therefore there is only partial commonality between the changes shown for NH_4^+ and NO_3^-. With the application of EQSAM4Clim, the surface concentration and burden of NH_4^+ decreases strongly, while the gas phase concentration of HNO_3 increases (c.f Table 6 and Figure 8).

For Europe (top panels), the EMEP observational annual total wet deposition values show that there is a rather constrained range in total oxidised N deposition (150-275 mgN/m²/year). This correlates with a rather homogeneous distribution of $[NO_3^-]$ shown in Sect. 4.3 ; a few high outliers are most likely affected by strong local NO_x emission sources. Although there are rather modest differences in cumulative wet deposition of $[NO_3^-]$ between Cy48r1 and Cy49r1, there is a marked improvement in the regional bias in the oxidised N wet deposition term, which decreases by 80% turning from positive to negative, albeit with no significant improvement in the (time-sensitive) correlation.

For the U.S. (middle panels), higher values of oxidised N deposition occur towards the East Coast as defined by the distribution of NO_x emissions (Figure 12). The range in CASTNET observational total wet deposition values is between 50-500 mgN/m²/year, exhibiting a strong longitudinal gradient. Although this gradient is captured rather well, there is typically an overestimation of between 100-200 mgN/m²/year for e.g. New York state and the surrounding regions in Cy48r1. For the Western U.S., observations provide the range of between 0-100 mgN/m²/year, with positive model biases of 100 mgN/m²/year for the North-Western states in both model versions. For the Southern U.S., Cy48r1 exhibits overestimates of 50-70 mgN/m²/year, which decreases noticeably in Cy49r1. There is a large positive bias in Cy48r1 of 130 mgN/m²/year which is improved in Cy49r1 decreasing by 23%. Again the Pearsons R value remains relatively unaffected showing the governing influence of the spatial distribution of the main point sources and a little effect on the forecasts itself (since IFS-COMPO is not employed here as a fully coupled forecasting system using data assimilation).

For South-East Asia (bottom panels), the range in the EANET observational total wet deposition values is between 50-800 mgN/m²/year, with the highest values of >2000 mgN/m²/year occurring on the Malaysian Coast. For Northern China, total wet deposition values of up to 400 mgN/m²/year occur, which is approximately half that observed near the Southern Coast and towards the East. The highest simulated wet deposition totals occur towards the South-West of China, correlating with high NO_x emissions. Comparing Cy48r1 and Cy49r1 shows that a marked decrease of 31% occurs between cycles, again with limited changes to the correlation.

6 Conclusions
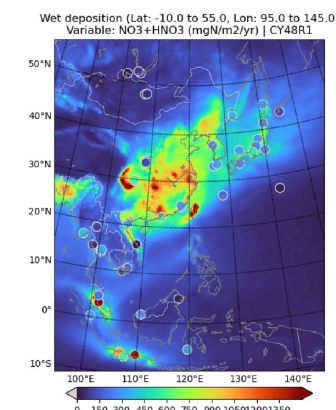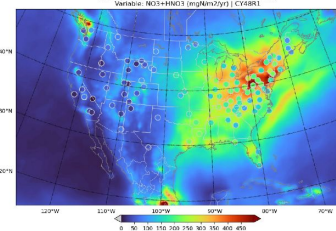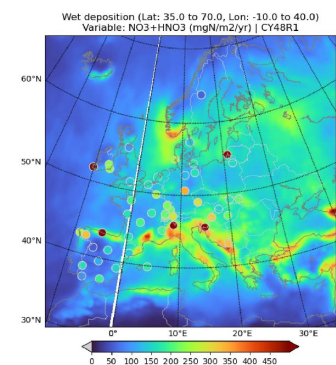
In this paper we build on the previous evaluations of the performance of IFS-COMPO Cy49r1 presented in Rémy et al. (2024), which evaluates the impact of EQSAM4Clim and its revised calculation of aerosol and cloud pH (Metzger et al., 2024) on its ability to improve air quality forecasts by segregating and investigating the individual inorganic components. To scrutinise its effect on the atmospheric composition, we compared the current operational IFS version, that contains a rather basic description of aerosol and cloud pH (Cy48r1), with the next operational IFS version, which uses EQSAM4Clim in combination with a unified wet scavenging approach and other developments (Cy49r1). Further improvements are also made with respect to both in-cloud and below cloud scavenging of soluble trace gases and aerosols through an implementation of updated parameterizations as detailed in Rémy et al. (2024).

We have shown that the most significant impacts of our IFS-COMPO updates concern the production efficacy of SIA and subsequent phase partitioning of reduced/oxidised nitrogen species. Comparing simulations with and without EQSAM4Clim, shows that changes in SIA are principally caused by altering the gas/aerosol partitioning. The verification and analysis has been presented for three dominant global source regions (Europe, the U.S. and South-East Asia), where we focus on evaluations of SIA surface concentration and wet deposition totals, by comparing against weekly/ammual observational composites for 2018.

For $SO_2(g)/SO_4^{2-}$, the conversion rate only exhibits moderate changes. For $SO_2(g)$, an increase in the global tropospheric burden of 7% indicates less phase transfer due to limitations in the uptake imposed by the increase in the solution pH. An increase in the gas phase production term of $H_2SO_4(g)$, which is subsequently scavenged, offsets a modest reduction in the aqueous phase production term. For surface $[SO_2(g)]$, this results in a lower mean annual bias for Europe with moderate correlation and a corresponding higher negative bias for the U.S. and with little correlation. No appreciable impact occurs for China, which shows a high positive bias of 11.5 µg/m³ with respect to CNEC and a correlation coefficient near zero. For $[SO_4^{2-}]$ there is an increase in both the tropospheric

Wet deposition (Lat: 35.0 to 70.0, Lon: -10.0 to 40.0)
Variable: NO3+HNO3 (mgN/m2/yr) | CY48R1

Wet deposition (Lat: 10.0 to 50.0, Lon: -130.0 to -60.0)
Variable: NO3+HNO3 (mgN/m2/yr) | CY48R1

Wet deposition (Lat: -10.0 to 55.0, Lon: 95.0 to 145.0)
Variable: NO3+HNO3 (mgN/m2/yr) | CY48R1

2004 burden and lifetime by one third due to the updates made to IFS-COMPO, with an associated reduction in the
2005 annual mean biases for Europe and the U.S. and increases in the corresponding correlation coefficients. However,
2006 for China there is a degradation in the performance which is associated with a positive annual mean bias and a
2007 decrease in the correlation coefficient.

2008 For $NH_3(g)/NH_4^+$ the changes are more substantial, resulting in beneficial improvements in the global modelling
2009 of reduced nitrogen. For $NH_3(g)$ the tropospheric burden almost doubles due to a halving of the conversion rate
2010 into NH_4^+, where more $NH_3(g)$ is directly deposited to the surface. For surface $[NH_3(g)]$, there is a contrasting
2011 change in the simulated weekly mean bias between Europe and the U.S. . For Europe, there is no significant
2012 improvement on the persistent high weekly mean biases, which increase by 10-25% during the spring and summer
2013 time despite all updates. For the U.S., the lower weekly $[NH_3(g)]$ has an associated low bias in the simulations,
2014 meaning the increase in the tropospheric burden improves the surface comparison markedly. For $[NH_4^+]$ in Europe,
2015 the application of EQSAM4Clim results in limited changes in the simulated weekly bias during the wintertime
2016 while significant reductions are found during summertime, with an associated increase in the annual mean
2017 correlation. For the U. S. and China, similar reductions in the annual mean bias of nearly 50% occur although the
2018 correlation is depreciated.

2019 For $HNO_3(g)/NO_3^-$ the changes are similar to those simulated for the $NH_3(g)/NH_4^+$ partitioning due to the
2020 speciation of the SIA being mainly linked via NH_4NO_3. The gas-phase production of $HNO_3(g)$ increases without
2021 an associated increase in the global tropospheric burden due to increases in the loss to surface via dry deposition.
2022 The application of EQSAM4Clim increases the fine aerosol component whilst reducing the coarse aerosol
2023 component, which reduces the fraction of $HNO_3(g)$ held in the particulate phase by 50%. For $HNO_3(g)$ in Europe
2024 and the U.S., there is a persistent negative bias which is changed to a significant positive bias. For $[NO_3^-]$,
2025 significant improvements in the annual mean biases occur across the globe as illustrated by the three chosen
2026 regions, which comes with improvements in the simulated correlation coefficients.

2027 EQSAM4Clim significantly influences wet deposition processes through its impact on aerosol loading and gas-
2028 aerosol partitioning. By altering the aerosol and cloud pH, the scheme modulates the chemical oxidation rates of
2029 precursor gases such as NH3, SO2 and HNO3. This, in turn, affects the formation and partitioning of SIA, their
2030 hygroscopic growth, and their subsequent removal of both dry and wet deposition pathways - including in-cloud
2031 and below-cloud scavenging. These changes also influence the aerosol radiative effects, both directly and
2032 indirectly, underscoring the interconnected role of thermodynamic aerosol modeling in atmospheric composition
2033 and deposition simulations.

2034 For the wet deposition component, changes in the SIA concentrations are qualitatively similar to the annual wet
2035 deposition totals, although regional changes are variable and species specific. For Europe, there are reductions in
2036 the simulated annual mean bias for all three chemical types, with oxidised N improving markedly. For the U.S.,
2037 the annual mean bias increases for wet S deposition, with decreases in biases for both reduced wet N and oxidised
2038 wet N. For South-East Asia, there is a marked improvement in wet S deposition, a moderate improvement in
2039 oxidised wet N and a degradation in reduced wet N. Overall, the recent improvements brought by EQSAM4Clim
2040 (Metzger et al., 2024) as applied here and in Rémy et al. (2024), shows that Cy49r1 is fit-for-purpose with respect
2041 to capturing regional particle concentration and the loss terms via wet deposition.

2042

2043

2044

2045

2046

2047

2048

2049

Appendix
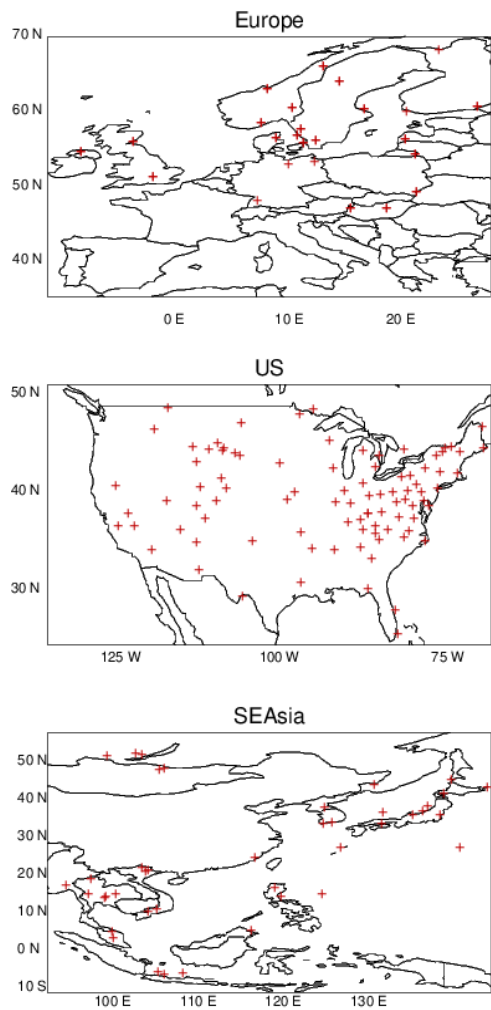
Figure A1 : The location of the observational sites used for evaluating the weekly surface concentration of SO$_2$ for Europe (top panel), the US (middle panel) and SEAsia (lower panel).

Author Contributions

JEW and SM were principal authors of the paper and produced most of the figures. SR conducted the IFS-COMPO simulations and performed the regional comparisons made against observational datasets for evaluating the deposition fluxes and was a co-PI of the CAMS35_2 development project. SM provided and integrated EQSAM4Clim for the more accurate calculation of pH using aerosols and clouds. VH updated the model towards Cy49r1, introduced technical updates with respect to the implementation of EQSAM4Clim and was co-PI of the

Formatted: Header

CY48R1 Surface SO$_2$ 2018O7   diff A 201
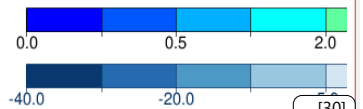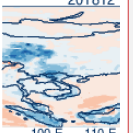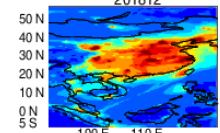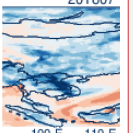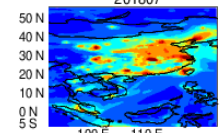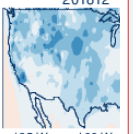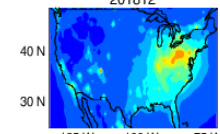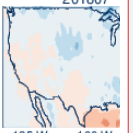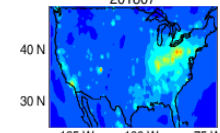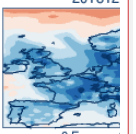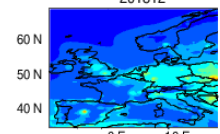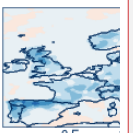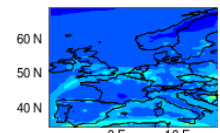
Deleted:

Moved up [4]: Fig.

Deleted: 1 except for HNO$_3$. Panel definitions : Diff A = (CY49R1_NOEQ4C - CY48R1)/CY48R1; Diff B = (CY49R1-CY48R1)/CY48R1 and Diff C = (CY49R1-CY49R1_NOEQ4C)/CY48R1.¶   [31]

Deleted: .

Deleted: CY49R1 and

Formatted: Right

CAMS35_2 development project. JF is a representative of the CAMS consortium under which this work was conducted.

Code availability

Model codes developed at ECMWF are the intellectual property of ECMWF and its member states, and therefore the IFS code is not publicly available. ECMWF member-state weather services and their approved partners will get access granted. Access to a version of the IFS (OpenIFS) that includes this experimental cycle may be obtained from ECMWF under an OpenIFS licence. More details at https://confluence.ecmwf.int/display/OIFS/About+OpenIFS

Data availability

The model codes created by ECMWF are considered intellectual property of ECMWF and its member states, and as such, the IFS code is not available to the public. Access to the IFS code is granted to ECMWF member-state weather services and their authorised partners. However, an open version of the IFS code, known as OpenIFS, which includes cycle CY43R3 IFS(AER) (Huijnen et al., 2022), can be obtained from ECMWF under an OpenIFS license. More details at https://confluence.ecmwf.int/display/OIFS/About+OpenIFS.

Competing Interests

The main author and one of the co-authors is a member of the editorial board of Geoscientific Model Development. The peer-review process was guided by an independent editor, and the authors also have no other competing interests to declare.

Acknowledgements

We acknowledge funding from the Copernicus Atmosphere Monitoring Service (CAMS), which is funded by the European Union's Copernicus Programme. We acknowledge the EMEP, EANET, AirNow, CASTNET, AMoN, AQeR and CNEMC monitoring networks for allowing access to surface observational data for SO_2, $SO_4^=$, NH_3, NH_4^+, HNO_3 and NO_3^-.

References

2130

2131

2132 van der A, R. J., Ding, J., and Eskes, H.: Monitoring European anthropogenic NO$_x$ emissions from space, Atmos.
2133 Chem. Phys., 24, 7523–7534, https://doi.org/10.5194/acp-24-7523-2024 , 2024.

2134 Aas, W., Mortier, A., Bowersox, V. *et al.* Global and regional trends of atmospheric sulfur. *Sci Rep* 9, 953,
2135 https://doi.org/10.1038/s41598-018-37304-0, 2019.

2136
2137 Aas, W., Fagerli, H., Alastuey, A., Cavalli, F., Degorska, A., Feigenspan, S., Brenna, H., Gliß, J., Heinesen, D.,
2138 Hueglin, C., Holubová, A., Jaffrezo, J.L., Mortier, A., Murovec, M., Putaud, J.P., Rüdiger, J., Simpson, D.,
2139 Solberg, S., Tsyro, S., Tørseth, K. and Yttri, K.E. : Trends in Air Pollution in Europe, 2000–2019. Aerosol Air
2140 Qual. Res. 24, 230237. https://doi.org/10.4209/aaqr.230237, 2024.

2141
2142 Ault, A.P : Aerosol Acidity: Novel Measurements and Implications for Atmospheric Chemistry, *Acc. Chem. Res,*
2143 53, 9, 1703–1714, https://doi.org/10.1021/acs.accounts.0c00303, 2020.

2144 Benish, S. E., Bash, J. O., Foley, K. M., Appel, K. W., Hogrefe, C., Gilliam, R., and Pouliot, G.: Long-term
2145 regional trends of nitrogen and sulfur deposition in the United States from 2002 to 2017, Atmos. Chem. Phys., 22,
2146 12749–12767, https://doi.org/10.5194/acp-22-12749-2022, 2022.

2147 Celik, S., Drewnick, F., Fachinger, F., Brooks, J., Darbyshire, E., Coe, H., Paris, J.-D., Eger, P. G., Schuladen, J.,
2148 Tadic, I., Friedrich, N., Dienhart, D., Hottmann, B., Fischer, H., Crowley, J. N., Harder, H., and Borrmann, S.:
2149 Influence of vessel characteristics and atmospheric processes on the gas and particle phase of ship emission
2150 plumes: in situ measurements in the Mediterranean Sea and around the Arabian Peninsula, Atmos. Chem. Phys.,
2151 20, 4713–4734, https://doi.org/10.5194/acp-20-4713-2020 , 2020.

2152 Chang, C.-T., Wang, L., Wang L-J, Liu, C-P, Yang, C-J, Huang, J-C., Wang, C-P, Lin N-H. and Lin, T-C.: On the
2153 seasonality of long-range transport of acidic pollutants in East Asia, Environ.Res.Letts., 17(9), doi:10.1088/1748-
2154 9326/ac8b99, 2022.

2155 Chen J, Cheng M, Krol M, de Vries W, Zhu Q, Liu X, Zhang F and Xu W (2023), Trends in anthropogenic
2156 ammonia emissions in China since 1980: A review of approaches and estimations. Front. Environ. Sci.
2157 11:1133753, doi: 10.3389/fenvs.2023.1133753.

2158 Croft, B., Lohmann, U., Martin, R. V., Stier, P., Wurzler, S., Feichter, J., Posselt, R., and Ferrachat, S.: Aerosol
2159 size-dependent below-cloud scavenging by rain and snow in the ECHAM5-HAM, Atmos. Chem. Phys., 9, 4653–
2160 4675, 2009.

2161 de Bruine, M., Krol, M., van Noije, T., Le Sager, P., and Rockmann, T.: The impact of precipitation evaporation
2162 on the atmospheric aerosol distribution in EC-Earth v3.2.0, Geosci. Model Dev., 11, 1443–1465, 2018.

2163 Dentener, F., Drevet, J., Lamarque, J. F.,Bey, I., Eickhout, B., Fiore, A. M., Hauglustaine, D., Horowitz, L. W.,
2164 Krol, M.,Kulshrestha, U. C., Lawrence, M., Galy-Lacaux, C., Rast, S., Shindell, D., Stevenson, D., Van Noije, T.,
2165 Atherton, C., Bell, N., Bergman, D., Butler, T., Cofala, J., Collins, B., Doherty, R., Ellingsen, K., Galloway, J.,
2166 Gauss, M., Montanaro, V., Muller, J. F., Pitari, G., Rodriguez, J.,Sand erson, M., Solmon, F., Strahan, S., Schultz,
2167 M., Sudo, K., Szopa, S., and Wild, O.: Nitrogen and sulfur deposition on regional and global scales:A multimodel
2168 evaluation, Global Biogeo. Cycles, 20, GB4003, doi:10.1029/2005GB002672 , 2006.

2169 Deschaseaux, E., O'Brien, J., Siboni, N., Petrou, K., and Seymour, J. R.: Shifts in dimethylated sulfur
2170 concentrations and microbiome composition in the red-tide causing dinoflagellate *Alexandrium minutum* during a
2171 simulated marine heatwave, Biogeosciences, 16, 4377–4391, https://doi.org/10.5194/bg-16-4377-2019 , 2019.

2172 Ding, J., van der A, R., Eskes, H., Dammers, E., Shephard, M., Wichink Kruit, R., Guevara, M., and Tarrason, L.:
2173 Ammonia emission estimates using CrIS satellite observations over Europe, EGUsphere [preprint],
2174 https://doi.org/10.5194/egusphere-2024-1073, 2024.

Du, H., Li, J., Wang, Z., Dao, X., Guo, S.,Wang, L., et al.: Effects of regional transport on haze in the NorthChina Plain: Transport of precursors or secondary inorganic aerosols.Geophysical Research Letters,47,e2020GL087461, https://doi.org/10.1029/2020GL087461, 2020.

Feick, G. and Hainer, R. M.: On the Thermal Decomposition of Ammonium Nitrate. Steady-state Reaction Temperatures and Reaction Rate, J. Am. Chem. Soc., 76, 22, 5860–5863, https://doi.org/10.1021/ja01651a096, 1954.

Fioletov, V., McLinden, C. A., Griffin, D., Theys, N., Loyola, D. G., Hedelt, P., Krotkov, N. A., and Li, C.: Anthropogenic and volcanic point source SO₂ emissions derived from TROPOMI on board Sentinel-5 Precursor: first results, Atmos. Chem. Phys., 20, 5591–5607, https://doi.org/10.5194/acp-20-5591-2020, , 2020.

Gao, J., Wei, Y., Guoliang, S., Yu, H., Zhang, Z., Song, S., Wang, W., Liang, D. and Feng, Y.: Roles of RH, aerosol pH and sources in concentrations of secondary inorganic aerosols, during different pollution periods, Atms. Environ., 241, 117770, https://doi.org/10.1016/j.atmosenv.2020.117770, 2020.

Ge, Y., Heal, M. R., Stevenson, D. S., Wind, P., and Vieno, M.: Evaluation of global EMEP MSC-W (rv4.34) WRF (v3.9.1.1) model surface concentrations and wet deposition of reactive N and S with measurements, Geosci. Model Dev., 14, 7021–7046, https://doi.org/10.5194/gmd-14-7021-2021, , 2021.

Giorgi, F. and Chameides, W. L.: Rainout lifetimes of highly soluble aerosols and gases as inferred from simulations with a general circulation model, J. Geophys. Res., 91, 367–376, 1986.

Goldberg, D. L., Anenberg, S. C., Kerr, G. H., Mohegh, A., Lu, Z., & Streets, D. G. : TROPOMI NO2 in the United States: A detailed look at the annual averages, weekly cycles, effects of temperature, and correlation with surface NO2 concentrations. Earth's Future, 9, e2020EF001665. https://doi.org/10.1029/2020EF001665, 2021.

Gu, B., Ju, X., Chang, J., Ge, Y. and Vitousek, P. M.: Integrated reactive nitrogen budgets and future trends in China, PNAS, 112 (28) 8792-8797, https://doi.org/10.1073/pnas.1510211112, 2015.

Hauglustaine, D. A., Balkanski, Y., and Schulz, M.: A global model simulation of present and future nitrate aerosols and their direct radiative forcing of climate, Atmos. Chem. Phys., 14, 11031–11063, https://doi.org/10.5194/acp-14-11031-2014, 2014.

He, H., Liang., X.-Z. and Wuebbles, D.J. : Effects of emissions change, climate change and long-range transport on regional modeling of future U.S. particulate matter pollution and speciation, Atmos. Environ., 179, 166-176, https://doi.org/10.1016/j.atmosenv.2018.02.020, 2018.

Holland, E. A., Braswell, B. H., Lamarque, J.-F., et al.: Variations in the predicted spatial distribution of atmospheric nitrogen deposition and their impact on carbon uptake by terrestrial ecosystems, J. Geophys. Res., 102, 15 849–15 866, 1997.

Huijnen, V., Flemming, J., Chabrillat, S., Errera, Q., Christophe, Y., Blechschmidt, A.-M., Richter, A., and Eskes, H.: C-IFS-CB05-BASCOE: stratospheric chemistry in the Integrated Forecasting System of ECMWF, Geosci. Model Dev., 9, 3071–3091, https://doi.org/10.5194/gmd-9-3071-2016, 2016.

Huijnen, V., Pozzer, A., Arteta, J., Brasseur, G., Bouarar, I., Chabrillat, S., Christophe, Y., Doumbia, T., Flemming, J., Guth, J., Josse, B., Karydis, V. A., Marécal, V., and Pelletier, S.: Quantifying uncertainties due to chemistry modelling – evaluation of tropospheric composition simulations in the CAMS model (cycle 43R1), Geosci. Model Dev., 12, 1725–1752, https://doi.org/10.5194/gmd-12-1725-2019, 2019.

Huijnen, V., Le Sager, P., Köhler, M. O., Carver, G., Rémy, S., Flemming, J., Chabrillat, S., Errera, Q., and van Noije, T.: OpenIFS/AC: atmospheric chemistry and aerosol in OpenIFS 43r3, Geosci. Model Dev., 15, 6221–6241, https://doi.org/10.5194/gmd-15-6221-2022, 2022.

von Glasow, R., Lawrence, M. G., Sander, R., and Crutzen, P. J.: Modeling the chemical effects of ship exhaust in the cloud-free marine boundary layer, Atmos. Chem. Phys., 3, 233–250, https://doi.org/10.5194/acp-3-233-2003, 2003.

Jayne, J. T., Davidovits, P., Worsnop, D. R., Zahniser, M. S., and Kolb, C. E.: Uptake of $SO_2(g)$ by Aqueous Surfaces as a Function of pH : The Effect of Chemical Reaction at the Interface, J. Phys. Chem., *J. Phys. Chem.*, 94, 15, 6041–6048, https://doi.org/10.1021/j100378a076, 1990.

Jiang, Z., Zhu, R., Miyazaki, K., McDonald, B. C., Klimont, Z., Zheng, B., et al. : Decadal variabilities in tropospheric nitrogen oxides over United States, Europe, and China. Journal of Geophysical Research: Atmospheres, 127, e2021JD035872. https://doi.org/10.1029/2021JD035872, 2022.

Kanakidou, M., Myriokefalitakis, S., Daskalakis, N., Fanourgakis, G., Nenes, A., Baker, A. R., K. Tsigaridis, K. and Mihalopoulos, N.: Past, Present and Future Atmospheric Nitrogen Deposition, J. Atmos Sci., 73(5): 2039–2047, doi: 10.1175/JAS-D-15-0278.1, 2016.

Liu, L., Zhang, X., Wong, A. Y. H., Xu, W., Liu, X., Li, Y., Mi, H., Lu, X., Zhao, L., Wang, Z., Wu, X., and Wei, J.: Estimating global surface ammonia concentrations inferred from satellite retrievals, Atmos. Chem. Phys., 19, 12051–12066, https://doi.org/10.5194/acp-19-12051-2019, 2019.

Liu, S., Valks, P., Pinardi, G., Xu, J., Chan, K. L., Argyrouli, A., Lutz, R., Beirle, S., Khorsandi, E., Baier, F., Huijnen, V., Bais, A., Donner, S., Dörner, S., Gratsea, M., Hendrick, F., Karagkiozidis, D., Lange, K., Piters, A. J. M., Remmers, J., Richter, A., Van Roozendael, M., Wagner, T., Wenig, M., and Loyola, D. G.: An improved TROPOMI tropospheric NO_2 research product over Europe, Atmos. Meas. Tech., 14, 7297–7327, https://doi.org/10.5194/amt-14-7297-2021, 2021.

Liu, S., Geng, G., Xioa, Q., Zheng, Y., Cheng, J.,and Zhang, Q.: Tracking Daily Concentrations of PM2.5 Chemical Composition in China since 2000, Environ. Sci. Technol., 56, 16517-16527, 2022.

Luo, G., Yu, F., and Schwab, J.: Revised treatment of wet scavenging processes dramatically improves GEOS-Chem 12.0.0 simulations of surface nitric acid, nitrate, and ammonium over the United States, *Geosci. Model Dev.*, 12, 3439–3447, https://doi.org/10.5194/gmd-12-3439-2019, 2019.

Metzger, S., Dentener, F., Pandis, S., and Lelieveld, J.: Gas/aerosol partitioning: 1. A computationally efficient model, J. Geophys. Res., 107, 4312, doi:10.1029/2001JD001102, 2002.

Metzger, S., Mihalopoulos, N., and Lelieveld, J.: Importance of mineral cations and organics in gas-aerosol partitioning of reactive nitrogen compounds: case study based on MINOS results, Atmos. Chemistry and Physics, 6, 2549–2567, https://doi.org/10.5194/acp-6-2549-2006, 2006.

Metzger, S., Steil, B., Abdelkader, M., Klingmüller, K., Xu, L., Penner, J. E., Fountoukis, C., Nenes, A., and Lelieveld, J.: Aerosol water parameterisation: a single parameter framework, Atmos. Chem. Phys., 16, 7213–7237, https://doi.org/10.5194/acp-16-7213-2016, 2016.

Metzger, S., Abdelkader, M., Steil, B., and Klingmüller, K.: Aerosol water parameterization: long-term evaluation and importance for climate studies, Atmos. Chem. Phys., 18, 16747–16774, https://doi.org/10.5194/acp-18-16747-2018, 2018.

Metzger, S., Rémy, S., Williams, J. E., Huijnen, V., and Flemming, J.: A computationally efficient parameterization of aerosol, cloud and precipitation pH for application at global and regional scale (EQSAM4Clim-v12), Geosci. Model Dev., 17, 5009–5021, https://doi.org/10.5194/gmd-17-5009-2024, 2024.

Myriokefalitakis, S., Bergas-Massó, E., Gonçalves-Ageitos, M., Pérez García-Pando, C., van Noije, T., Le Sager, P., Ito, A., Athanasopoulou, E., Nenes, A., Kanakidou, M., Krol, M. C., and Gerasopoulos, E.: Multiphase processes in the EC-Earth model and their relevance to the atmospheric oxalate, sulfate, and iron cycles, Geosci. Model Dev., 15, 3079–3120, https://doi.org/10.5194/gmd-15-3079-2022, 2022.

Pan, D., Mauzerall, D.L., Wang, R., Guo, X., Puchalski, M., Guo, Y., Song, S., Tong, D., Sullivan, A. P., Schichtel, B. A., Collet Jr, J. L. and Zondlo, M. A.: Regime shift in secondary inorganic aerosol formation and nitrogen deposition in the rural United States. Nat. Geosci. https://doi.org/10.1038/s41561-024-01455-9 , 2024.

Peuch, V-H., Engelen, R., Rixen, M., Dee, D., Flemming, J., Suttie, M., Ades, M., Agustí-Panareda, A., Ananasso, C., Andersson, E., Armstrong, D., Barré, J., Nicolas Bousserez, N., Dominguez, J. J., Garrigues, S., Inness, A., Jones, L., Kipling, Z., Letertre-Danczak, J., Parrington, M., Razinger, M., Ribas, R., Vermoote, S., Yang, X., Simmons, A., Garcés de Marcilla, J., and Thépaut, J.-N. : The Copernicus Atmosphere Monitoring Service: From Research to Operations, BAMS, E2650–E2668, https://doi.org/10.1175/BAMS-D-21-0314.1, 2024.

Reay, D. S., Dentener, F., Smith, P., Grace, J., and Feely, R. A.: Global nitrogen deposition and carbon sinks, Nat. Geosci., 1, 430–437, 2008.

Rémy, S., Kipling, Z., Flemming, J., Boucher, O., Nabat, P., Michou, M., Bozzo, A., Ades, M., Huijnen, V., Benedetti, A., Engelen, R., Peuch, V.-H., and Morcrette, J.-J.: Description and evaluation of the tropospheric aerosol scheme in the European Centre for Medium-Range Weather Forecasts (ECMWF) Integrated Forecasting System (IFS-AER, cycle 45R1), Geosci. Model Dev., 12, 4627–4659, https://doi.org/10.5194/gmd-12-4627-2019, 2019.

Rémy, S., Kipling, Z., Huijnen, V., Flemming, J., Nabat, P., Michou, M., Ades, M., Engelen, R., and Peuch, V.-H.: Description and evaluation of the tropospheric aerosol scheme in the Integrated Forecasting System (IFS-AER, cycle 47R1) of ECMWF, Geosci. Model Dev., 15, 4881–4912, https://doi.org/10.5194/gmd-15-4881-2022, 2022.

Renner, E and Wolke, R.: Modelling the formation and atmospheric transport of secondary inorganic aerosols with special attention to regions with high ammonia emissions, Atmos. Environ., 44(15), https://doi.org/10.1016/j.atmosenv.2010.02.018, 2010.

Rémy, S., Metzger, S., Huijnen, V, Williams, J. E. and Flemming, J.: Representation and impact of aerosol acidity in the ECMWF IFS-COMPO cycle 49R1 through the integration of EQSAM4Clim vXX, *Geosci. Model Dev.*, 2024.

Seinfeld, J. and Pandis, S.: Atmospheric Chemistry and Physics: From Air Pollution to Climate Change - second edition, New Jersey: John Wiley and Sons, 2006.

Shah, V., Jacob, D. J., Moch, J. M., Wang, X., and Zhai, S.: Global modeling of cloud water acidity, precipitation acidity, and acid inputs to ecosystems, *Atmos. Chem. Phys.*, 20, 12 223–12 245, https://doi.org/10.5194/acp-20-12223-2020, 2020.

Sharma, S. K., Singh, A. K., Saud, T., Mandal, T. K., Saxena, M., Singh, S., Ghosh, S. K., and Raha, S.: Measurement of ambient NH_3 over Bay of Bengal during W_ICARB Campaign, *Ann. Geophys.*, 30, 371–377, https://doi.org/10.5194/angeo-30-371-2012, 2012.

Sharma, S., Chandra, M. and Kota, S.H.: Health Effects Associated with $PM_{2.5}$: a Systematic Review, *Curr Pollution Rep* **6**, 345–367, https://doi.org/10.1007/s40726-020-00155-3, 2020.

Shephard, M. W., Cady-Pereira, K. E., Luo, M., Henze, D. K., Pinder, R. W., Walker, J. T., Rinsland, C. P., Bash, J. O., Zhu, L., Payne, V. H., and Clarisse, L.: TES ammonia retrieval strategy and global observations of the spatial and seasonal variability of ammonia, Atmos. Chem. Phys., 11, 10743–10763, https://doi.org/10.5194/acp-11-10743-2011, 2011.

Shi, G., Xu, J., Shi, X., Liu, B., Bi, X.,Xiao, Z., et al: Aerosol pH dynamics during haze periods in an urban environment in China: Use of detailed, hourly, speciated observations to study the role of ammonia availability and secondary aerosol formation and urban environment.Journal of Geophysical Research:Atmospheres,124, 9730–9742. https://doi.org/10.1029/2018JD029976, 2019.

Sindelarova, K., Markova, J., Simpson, D., Huszar, P., Karlicky, J., Darras, S., and Granier, C.: High-resolution biogenic global emission inventory for the time period 2000–2019 for air quality modelling, Earth Syst. Sci. Data, 14, 251–270, https://doi.org/10.5194/essd-14-251-2022, 2022.

Simpson, D, Aas, W., Bartnicki, J., Berge, H., Bleeker, A., Cuvelier, C., Dentener, F., Dore, A. Erisman, J.-W., Fagerli, H., Flechard, C., Hertel, O., Jaarsveld, H., Jenkin, M.E., Schaap, M. Smeena, V.S., Thunis, P., Vautard, R. and Vieno, M.: Atmospheric transport and deposition of reactive nitrogen in Europe. The European Nitrogen Assessment, 298-316, doi:10.1017/CBO9780511976988.017, 2010.

Simpson, R. M. C., S. G. Howell,B. W. Blomquist, A. D. Clarke, and B. J.Huebert, Dimethyl sulfide: Lessimportant than long-range transport as a source of sulfate to the remote tropical Pacific marine boundary layer,J. Geophys. Res. Atmos., 119, 9142–9167, doi:10.1002/2014JD021643 , 2014.

Soulie, A., Granier, C., Darras, S., Zilbermann, N., Doumbia, T., Guevara, M., Jalkanen, J.-P., Keita, S., Liousse, C., Crippa, M., Guizzardi, D., Hoesly, R., and Smith, S.: Global Anthropogenic Emissions (CAMS-GLOB-ANT) for the Copernicus Atmosphere Monitoring Service Simulations of Air Quality Forecasts and Reanalyses, Earth Syst. Sci. Data, 16, 2261–2279, https://doi.org/10.5194/essd-16-2261-2024 , 2024,

Sun, Y. , Guo, G., Li, Y., Luo, G., Li, L., Yuan, H., Mur, L. A. J. and Guo, S.: Negative effects of the simulated nitrogen deposition on plant phenolic metabolism: A meta-analysis, *Sci. Total Environ.,* 19, 137–142, 2020.

Tan, J., Fu, J. S., Dentener, F., Sun, J., Emmons, L., Tilmes, S., Sudo, K., Flemming, J., Jonson, J. E., Gravel, S., Bian, H., Davila, Y., Henze, D. K., Lund, M. T., Kucsera, T., Takemura, T., and Keating, T.: Multi-model study of HTAP II on sulphur and nitrogen deposition, *Atmos. Chem. Phys.*, 18, 6847–6866, https://doi.org/10.5194/acp-18-6847-2018 , 2018.

Tang, Y. S., Flechard, C. R., Dämmgen, U., Vidic, S., Djuricic, V., Mitosinkova, M., Uggerud, H. T., Sanz, M. J., Simmons, I., Dragosits, U., Nemitz, E., Twigg, M., van Dijk, N., Fauvel, Y., Sanz, F., Ferm, M., Perrino, C., Catrambone, M., Leaver, D., Braban, C. F., Cape, J. N., Heal, M. R., and Sutton, M. A.: Pan-European rural monitoring network shows dominance of NH_3 gas and NH_4NO_3 aerosol in inorganic atmospheric pollution load, Atmos. Chem. Phys., 21, 875–914, https://doi.org/10.5194/acp-21-875-2021 , 2021.

Tichý, O., Eckhardt, S., Balkanski, Y., Hauglustaine, D., and Evangeliou, N.: Decreasing trends of ammonia emissions over Europe seen from remote sensing and inverse modelling, Atmos. Chem. Phys., 23, 15235–15252, https://doi.org/10.5194/acp-23-15235-2023, 2023.

Tørseth, K., Aas, W., Breivik, K., Fjæraa, A. M., Fiebig, M., Hjellbrekke, A. G., Lund Myhre, C., Solberg, S., and Yttri, K. E.: Introduction to the European Monitoring and Evaluation Programme (EMEP) and observed atmospheric composition change during 1972–2009, Atmos. Chem. Phys., 12, 5447–5481, https://doi.org/10.5194/acp-12-5447-2012, 2012.

Turnock, S. T., Mann, G. W.,Woodhouse, M. T., Dalvi, M.,O'Connor, F. M., Carslaw, K. S., and Spracklen, D. V.: The impact of changes in cloud water pH on aerosol radiative forcing, Geophys. Res. Lett., 46, 4039–4048. https://doi.org/10.1029/2019GL082067, 2019.

Ting. Y.C., Young, L.H., Lin TH, Tsay, S.C., Chang, K.E. and Hsiao, T.C: Quantifying the impacts of $PM_{2.5}$ constituents and relative humidity on visibility impairment in a suburban area of eastern Asia using long-term in-situ measurements. Sci Total Environ. 2022 Apr 20;818:151759. doi: 10.1016/j.scitotenv.2021.151759. Epub 2021 Nov 22. PMID: 34822889, 2022.

Tørseth, K., Aas, W., Breivik, K., Fjaeraa, A. M., Fiebig, M., Hjellbrekke, A. G., Lund-Myrhe, C., Solberg, S. and Yttri, K. E.: Introduction to the European Monitoring and Evaluation Programme (EMEP) and observed atmospheric composition change during 1972–2009, Atmos. Chem. Phys., 12, pp. 5447-5481, 2012.

van Noije, T. P. C., Le Sager, P., Segers, A. J., van Velthoven, P. F. J., Krol, M. C., Hazeleger, W., Williams, A. G., and Chambers, S. D.: Simulation of tropospheric chemistry and aerosols with the climate model EC-Earth, Geosci. Model Dev., 7, 2435–2475, https://doi.org/10.5194/gmd-7-2435-2014, 2014.

Verheggen, B., Cozic, J., Weingartner, E., Bower, K., Mertes, S., Connolly, P., Gallagher, M., Flynn, M., Choularton, T., and Baltensperger, U.: Aerosol partitioning between the interstitial and the condensed phase in mixed-phase clouds, Journal of Geophysical Research: Atmospheres, 112, https://doi.org/https://doi.org/10.1029/2007JD008714, 2007.

Verstraeten, W. W., Boersma, K. F. , Douros, J., Williams, J. E., Eskes, H., Liu, F., Beirle, S. and Delcloo, A.: Top-Down NOX Emissions of European Cities Based on the Downwind Plume of Modelled and Space-Borne Tropospheric NO2 Columns, Sensors, 18, 2893, http://dx.doi.org/10.3390/s18092893, 2018.

Vestreng, V., Myhre, G., Fagerli, H., Reis, S., and Tarrasón, L.: Twenty-five years of continuous sulphur dioxide emission reduction in Europe, Atmos. Chem. Phys., 7, 3663–3681, https://doi.org/10.5194/acp-7-3663-2007, 2007.

Vieno, M., Heal, M. R., Hallsworth, S., Famulari, D., Doherty, R. M., Dore, A. J., Tang, Y. S., Braban, C. F., Leaver, D., Sutton, M. A., and Reis, S.: The role of long-range transport and domestic emissions in determining atmospheric secondary inorganic particle concentrations across the UK, Atmos. Chem. Phys., 14, 8435–8447, https://doi.org/10.5194/acp-14-8435-2014, 2014.

Vinken, G. C. M., Boersma, K. F., Jacob, D. J., & Meijer, E. W.: Accounting for non-linear chemistry of ship plumes in the GEOS-Chem global chemistry transport model. Atmospheric Chemistry and Physics, 11(22), 11707-11722. https://doi.org/10.5194/acp-11-11707-2011, 2011.

Wang, J., Xu, J., He, Y., Chen, Y., and Meng, F.: Long range transport of nitrate in the low atmosphere over Northeast Asia, Atmos. Environ., 144, 315-324, https://doi.org/10.1016/j.atmosenv.2016.08.084, 2016.

Wang, R., Pan, D., Guo, X., Sun, K., Clarisse, L., Van Damme, M., Coheur, P.-F., Clerbaux, C., Puchalski, M., and Zondlo, M. A.: Bridging the spatial gaps of the Ammonia Monitoring Network using satellite ammonia measurements, Atmos. Chem. Phys., 23, 13217–13234, https://doi.org/10.5194/acp-23-13217-2023, 2023.

Williams., J. E., van der Swaluw, E., de Vries, W. J., Sauter, F. J., van Pul, W.A.J. and Hoogerbrugge, R.: Modelling the future distribution of ammonium nitrate concentrations in The Netherlands for 2020: The sensitivity to meteorological parameters, Atmos. Environm., Volume: 115, 278-285, doi: 10.1016/j.atmosenv.2015.06.001, 2015.

Williams, J. E ., Huijnen, V., Bouarar, I., Meziane, M., Schreurs, T., Pelletier, S., Marécal, V., Josse, B., and Flemming, J.: Regional evaluation of the performance of the global CAMS chemical modeling system over the United States (IFS cycle 47R1), Geosci. Model Dev., 15, 4657–4687, https://doi.org/10.5194/gmd-15-4657-2022, 2022.

Ye, X., Arab, P., Ahmadov, R., James, E., Grell, G. A., Pierce, B., Kumar, A., Makar, P., Chen, J., Davignon, D., Carmichael, G. R., Ferrada, G., McQueen, J., Huang, J., Kumar, R., Emmons, L., Herron-Thorpe, F. L., Parrington, M., Engelen, R., Peuch, V.-H., da Silva, A., Soja, A., Gargulinski, E., Wiggins, E., Hair, J. W., Fenn, M., Shingler, T., Kondragunta, S., Lyapustin, A., Wang, Y., Holben, B., Giles, D. M., and Saide, P. E.: Evaluation and intercomparison of wildfire smoke forecasts from multiple modeling systems for the 2019 Williams Flats fire, Atmos. Chem. Phys., 21, 14427–14469, https://doi.org/10.5194/acp-21-14427-2021, 2021

Zhang, L., Jacob, D. J., Knipping, E. M., Kumar, N., Munger, J. W., Carouge, C. C., van Donkelaar, A., Wang, Y. X., and Chen, D.: Nitrogen deposition to the United States: distribution, sources, and processes, Atmos. Chem. Phys., 12, 4539–4554, https://doi.org/10.5194/acp-12-4539-2012, 2012.

Page 7: [1] Deleted   **J.E. Williams**   **12/06/2025 14:07:00**

Page 7: [2] Deleted   **J.E. Williams**   **12/06/2025 14:07:00**

Page 7: [2] Deleted   **J.E. Williams**   **12/06/2025 14:07:00**

Page 7: [2] Deleted   **J.E. Williams**   **12/06/2025 14:07:00**

Page 7: [2] Deleted   **J.E. Williams**   **12/06/2025 14:07:00**

Page 7: [2] Deleted   **J.E. Williams**   **12/06/2025 14:07:00**

Page 7: [2] Deleted   **J.E. Williams**   **12/06/2025 14:07:00**

Page 7: [3] Deleted   **J.E. Williams**   **12/06/2025 14:07:00**

Page 7: [3] Deleted   **J.E. Williams**   **12/06/2025 14:07:00**

Page 7: [4] Deleted   **J.E. Williams**   **12/06/2025 14:07:00**

Page 7: [4] Deleted   **J.E. Williams**   **12/06/2025 14:07:00**

Page 7: [4] Deleted   **J.E. Williams**   **12/06/2025 14:07:00**

Page 7: [5] Deleted   **J.E. Williams**   **12/06/2025 14:07:00**

Page 7: [6] Deleted   **J.E. Williams**   **12/06/2025 14:07:00**

Page 7: [6] Deleted   **J.E. Williams**   **12/06/2025 14:07:00**

Page 7: [6] Deleted   **J.E. Williams**   **12/06/2025 14:07:00**

| Page 7: [6] Deleted | J.E. Williams | 12/06/2025 14:07:00 |

| Page 7: [7] Deleted | J.E. Williams | 12/06/2025 14:07:00 |

| Page 7: [7] Deleted | J.E. Williams | 12/06/2025 14:07:00 |

| Page 7: [7] Deleted | J.E. Williams | 12/06/2025 14:07:00 |

| Page 7: [7] Deleted | J.E. Williams | 12/06/2025 14:07:00 |

| Page 7: [7] Deleted | J.E. Williams | 12/06/2025 14:07:00 |

| Page 7: [7] Deleted | J.E. Williams | 12/06/2025 14:07:00 |

| Page 7: [7] Deleted | J.E. Williams | 12/06/2025 14:07:00 |

| Page 11: [8] Deleted | J.E. Williams | 12/06/2025 14:07:00 |

| Page 11: [8] Deleted | J.E. Williams | 12/06/2025 14:07:00 |

| Page 11: [8] Deleted | J.E. Williams | 12/06/2025 14:07:00 |

| Page 11: [8] Deleted | J.E. Williams | 12/06/2025 14:07:00 |

| Page 11: [8] Deleted | J.E. Williams | 12/06/2025 14:07:00 |

| Page 11: [8] Deleted | J.E. Williams | 12/06/2025 14:07:00 |

| Page 11: [9] Deleted | J.E. Williams | 12/06/2025 14:07:00 |

| Page 11: [9] Deleted | J.E. Williams | 12/06/2025 14:07:00 |

| Page 11: [9] Deleted | J.E. Williams | 12/06/2025 14:07:00 |

Page 11: [9] Deleted	J.E. Williams	12/06/2025 14:07:00
Page 11: [10] Deleted	J.E. Williams	12/06/2025 14:07:00
Page 11: [10] Deleted	J.E. Williams	12/06/2025 14:07:00
Page 11: [10] Deleted	J.E. Williams	12/06/2025 14:07:00
Page 11: [10] Deleted	J.E. Williams	12/06/2025 14:07:00
Page 11: [10] Deleted	J.E. Williams	12/06/2025 14:07:00
Page 11: [10] Deleted	J.E. Williams	12/06/2025 14:07:00
Page 11: [10] Deleted	J.E. Williams	12/06/2025 14:07:00
Page 11: [11] Deleted	J.E. Williams	12/06/2025 14:07:00
Page 11: [11] Deleted	J.E. Williams	12/06/2025 14:07:00
Page 11: [11] Deleted	J.E. Williams	12/06/2025 14:07:00
Page 11: [11] Deleted	J.E. Williams	12/06/2025 14:07:00
Page 11: [11] Deleted	J.E. Williams	12/06/2025 14:07:00
Page 13: [12] Deleted	J.E. Williams	12/06/2025 14:07:00
Page 13: [13] Deleted	J.E. Williams	12/06/2025 14:07:00
Page 13: [14] Deleted	J.E. Williams	12/06/2025 14:07:00
Page 16: [15] Deleted	J.E. Williams	12/06/2025 14:07:00

Page 18: [16] Deleted	J.E. Williams	12/06/2025 14:07:00
Page 20: [17] Deleted	J.E. Williams	12/06/2025 14:07:00
Page 22: [18] Deleted	J.E. Williams	12/06/2025 14:07:00
Page 22: [18] Deleted	J.E. Williams	12/06/2025 14:07:00
Page 22: [18] Deleted	J.E. Williams	12/06/2025 14:07:00
Page 22: [19] Deleted	J.E. Williams	12/06/2025 14:07:00
Page 22: [19] Deleted	J.E. Williams	12/06/2025 14:07:00
Page 22: [19] Deleted	J.E. Williams	12/06/2025 14:07:00
Page 23: [20] Deleted	J.E. Williams	12/06/2025 14:07:00
Page 26: [21] Deleted	J.E. Williams	12/06/2025 14:07:00
Page 30: [22] Deleted	J.E. Williams	12/06/2025 14:07:00
Page 30: [22] Deleted	J.E. Williams	12/06/2025 14:07:00
Page 30: [23] Deleted	J.E. Williams	12/06/2025 14:07:00
Page 30: [23] Deleted	J.E. Williams	12/06/2025 14:07:00
Page 30: [24] Deleted	J.E. Williams	12/06/2025 14:07:00
Page 30: [24] Deleted	J.E. Williams	12/06/2025 14:07:00

| Page 30: [24] Deleted | J.E. Williams | 12/06/2025 14:07:00 |

| Page 30: [24] Deleted | J.E. Williams | 12/06/2025 14:07:00 |

| Page 30: [24] Deleted | J.E. Williams | 12/06/2025 14:07:00 |

| Page 30: [24] Deleted | J.E. Williams | 12/06/2025 14:07:00 |

| Page 30: [25] Deleted | J.E. Williams | 12/06/2025 14:07:00 |

| Page 30: [25] Deleted | J.E. Williams | 12/06/2025 14:07:00 |

| Page 30: [25] Deleted | J.E. Williams | 12/06/2025 14:07:00 |

| Page 30: [26] Deleted | J.E. Williams | 12/06/2025 14:07:00 |

| Page 30: [27] Deleted | J.E. Williams | 12/06/2025 14:07:00 |

| Page 30: [27] Deleted | J.E. Williams | 12/06/2025 14:07:00 |

| Page 30: [27] Deleted | J.E. Williams | 12/06/2025 14:07:00 |

| Page 30: [27] Deleted | J.E. Williams | 12/06/2025 14:07:00 |

| Page 30: [27] Deleted | J.E. Williams | 12/06/2025 14:07:00 |

| Page 30: [27] Deleted | J.E. Williams | 12/06/2025 14:07:00 |

| Page 30: [28] Deleted | J.E. Williams | 12/06/2025 14:07:00 |

| Page 30: [28] Deleted | J.E. Williams | 12/06/2025 14:07:00 |

Page 30: [28] Deleted	J.E. Williams	12/06/2025 14:07:00

Page 30: [28] Deleted	J.E. Williams	12/06/2025 14:07:00

Page 30: [28] Deleted	J.E. Williams	12/06/2025 14:07:00

Page 30: [29] Deleted	J.E. Williams	12/06/2025 14:07:00

Page 30: [29] Deleted	J.E. Williams	12/06/2025 14:07:00

Page 32: [30] Deleted	J.E. Williams	12/06/2025 14:07:00

Page 32: [31] Deleted	J.E. Williams	12/06/2025 14:07:00

Page 36: [32] Formatted	J.E. Williams	12/06/2025 14:07:00

Font: 10 pt

Page 36: [32] Formatted	J.E. Williams	12/06/2025 14:07:00

Font: 10 pt

Page 36: [32] Formatted	J.E. Williams	12/06/2025 14:07:00

Font: 10 pt

Page 36: [32] Formatted	J.E. Williams	12/06/2025 14:07:00

Font: 10 pt

Page 36: [33] Formatted	J.E. Williams	12/06/2025 14:07:00

Font: 10 pt

Page 36: [33] Formatted	J.E. Williams	12/06/2025 14:07:00

Font: 10 pt

Page 36: [33] Formatted	J.E. Williams	12/06/2025 14:07:00

Font: 10 pt

Page 36: [34] Formatted	J.E. Williams	12/06/2025 14:07:00

Font: 10 pt

Page 36: [34] Formatted	J.E. Williams	12/06/2025 14:07:00

Font: 10 pt

Page 36: [34] Formatted	J.E. Williams	12/06/2025 14:07:00

Font: 10 pt

Page 36: [34] Formatted	J.E. Williams	12/06/2025 14:07:00

Font: 10 pt

Page 36: [34] Formatted	J.E. Williams	12/06/2025 14:07:00

Font: 10 pt

Page 36: [34] Formatted	J.E. Williams	12/06/2025 14:07:00

Font: 10 pt

Page 36: [34] Formatted	J.E. Williams	12/06/2025 14:07:00

Font: 10 pt

Page 36: [34] Formatted	J.E. Williams	12/06/2025 14:07:00

Font: 10 pt

Page 36: [34] Formatted	J.E. Williams	12/06/2025 14:07:00

Font: 10 pt

Page 36: [34] Formatted	J.E. Williams	12/06/2025 14:07:00

Font: 10 pt

Page 36: [34] Formatted	J.E. Williams	12/06/2025 14:07:00

Font: 10 pt

Page 36: [34] Formatted	J.E. Williams	12/06/2025 14:07:00

Font: 10 pt

Page 36: [34] Formatted	J.E. Williams	12/06/2025 14:07:00

Font: 10 pt

Page 36: [34] Formatted	J.E. Williams	12/06/2025 14:07:00

Font: 10 pt

Page 36: [34] Formatted	J.E. Williams	12/06/2025 14:07:00

Font: 10 pt

| Page 36: [34] Formatted | J.E. Williams | 12/06/2025 14:07:00 |

Font: 10 pt

| Page 36: [34] Formatted | J.E. Williams | 12/06/2025 14:07:00 |

Font: 10 pt

| Page 36: [34] Formatted | J.E. Williams | 12/06/2025 14:07:00 |

Font: 10 pt

| Page 36: [34] Formatted | J.E. Williams | 12/06/2025 14:07:00 |

Font: 10 pt

| Page 36: [34] Formatted | J.E. Williams | 12/06/2025 14:07:00 |

Font: 10 pt

| Page 36: [34] Formatted | J.E. Williams | 12/06/2025 14:07:00 |

Font: 10 pt

| Page 36: [34] Formatted | J.E. Williams | 12/06/2025 14:07:00 |

Font: 10 pt

| Page 36: [34] Formatted | J.E. Williams | 12/06/2025 14:07:00 |

Font: 10 pt

| Page 36: [34] Formatted | J.E. Williams | 12/06/2025 14:07:00 |

Font: 10 pt

| Page 36: [35] Formatted | J.E. Williams | 12/06/2025 14:07:00 |

Font: 10 pt

| Page 36: [35] Formatted | J.E. Williams | 12/06/2025 14:07:00 |

Font: 10 pt

| Page 36: [35] Formatted | J.E. Williams | 12/06/2025 14:07:00 |

Font: 10 pt

| Page 36: [36] Formatted | J.E. Williams | 12/06/2025 14:07:00 |

Font: 10 pt

| Page 36: [36] Formatted | J.E. Williams | 12/06/2025 14:07:00 |

Font: 10 pt

| **Page 36: [36] Formatted** | **J.E. Williams** | **12/06/2025 14:07:00** |

Font: 10 pt

| **Page 36: [37] Formatted** | **J.E. Williams** | **12/06/2025 14:07:00** |

Font: 10 pt

| **Page 36: [37] Formatted** | **J.E. Williams** | **12/06/2025 14:07:00** |

Font: 10 pt

| **Page 36: [37] Formatted** | **J.E. Williams** | **12/06/2025 14:07:00** |

Font: 10 pt

| **Page 36: [38] Formatted** | **J.E. Williams** | **12/06/2025 14:07:00** |

Font: 10 pt

| **Page 36: [38] Formatted** | **J.E. Williams** | **12/06/2025 14:07:00** |

Font: 10 pt

| **Page 36: [38] Formatted** | **J.E. Williams** | **12/06/2025 14:07:00** |

Font: 10 pt

| **Page 36: [39] Formatted** | **J.E. Williams** | **12/06/2025 14:07:00** |

Font: 10 pt

| **Page 36: [39] Formatted** | **J.E. Williams** | **12/06/2025 14:07:00** |

Font: 10 pt

| **Page 36: [39] Formatted** | **J.E. Williams** | **12/06/2025 14:07:00** |

Font: 10 pt